Chemical Science

ROYAL SOCIETY OF CHEMISTRY

REVIEW

View Article Online
View Journal | View Issue

Cite this: *Chem. Sci.*, 2026, **17**, 36

Robust π-conjugated radical cations

Shilong Su [a] and Qian Miao *[ab]

π-Conjugated radical cations, open-shell species carrying a positive charge, serve as charge carriers in p-type organic semiconductors, underpinning the operation of various organic electronic devices. Although they are traditionally perceived as highly reactive and challenging to isolate under ambient conditions, recent advances in electronic and steric stabilization have enabled the isolation and full characterization of a number of robust π-conjugated radical cations. This review provides a comprehensive overview of fully characterized π-conjugated radical cations, with particular emphasis on species identified *via* single-crystal X-ray crystallography within the last two decades. We highlight structural features and stabilization strategies that enable ambient stability, and explore structure–property relationships critical to their application in organic electronic materials, indicating the potential to enhance material stability and improve device performance. Based on this analysis, we assess the current state of the field and outline promising future directions.

Received 1st September 2025
Accepted 18th November 2025

DOI: 10.1039/d5sc06726j

rsc.li/chemical-science

1. Introduction

π-Conjugated radical cations are open-shell species that carry a positive charge, typically generated by oxidation of a neutral, closed-shell π-conjugated system.[1] They play a central role in organic electronic materials and devices because the doped states of p-type organic semiconductors are commonly associated with radical cations.[2] As a result, most organic conductors rely on π-conjugated radical cation salts, and the operation of various organic electronic devices depends on the controlled generation of π-conjugated radical cations. This is well illustrated by early examples of conducting radical cation salts, as shown in Fig. 1. Oxidation of tetrathiafulvalene (TTF) with Cl_2 results in the radical cation salt $TTF^{\bullet+}Cl^-$,[3] which exhibits a room-temperature conductivity of 0.27 ± 0.1 S cm^{-1} in microcrystalline form.[4] Similarly, electrochemical oxidation of bis(ethylenedithiolo)tetrathiafulvalene (BEDT-TTF) in the presence of CuSCN produces the crystal of $(BEDT\text{-}TTF)_2^{\bullet+}Cu(SCN)_2^-$, in which two BEDT-TTF molecules dimerize through short S···S contacts and share a single unpaired electron. The resulting single crystal displays a room-temperature conductivity of 14 S cm^{-1} and becomes a superconductor at 10.4 K under ambient pressure.[5] The third example is the perchlorate salt of the tetrakis(methylthio)pyrene (TMTP) radical cation, $(TMTP)_2^{\bullet+}ClO_4^-$, which exhibits an exceptionally high room-temperature conductivity in the range of 156 to 667 S cm^{-1}.[6,7] Consistent with this behavior, the neutral TMTP molecule functions as an organic semiconductor, recently reported to exhibit a remarkably high hole mobility of 32 $cm^2 V^{-1} s^{-1}$ in single-crystal organic field-effect transistors (OFETs).[8]

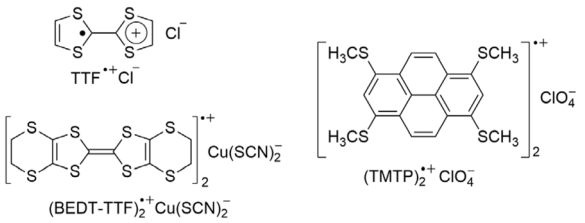

Fig. 1 Early examples of organic conductors and superconductors based on radical cation salts.

The unique electronic structures of π-conjugated radical cations—combining both radical and ionic characteristics—give rise not only to electrical conductivity[9] but also to magnetic[10] and optical properties[11,12] due to their unpaired spin densities. These features open avenues for unconventional applications,[13–16] such as doublet emission in organic light-emitting diodes (OLEDs) with 100% internal quantum efficiency.[17] Despite their importance, π-conjugated radical cations typically exhibit high reactivity, which often results in difficulties in isolating them in pure form and limits their detailed structural and spectroscopic characterization. Furthermore, their paramagnetic nature renders NMR signals undetectable. Consequently, full characterization of these species typically requires single-crystal X-ray crystallography. Over the past two decades, advances in electronic and steric stabilization have enabled the isolation of a number of ambient-stable π-conjugated radical cations. This review highlights these advances and shows how the full characterization of these stable systems has revealed key structural motifs governing stability. These

[a]*Department of Chemistry, The Chinese University of Hong Kong, Shatin, New Territories, Hong Kong, China. E-mail: miaoqian@cuhk.edu.hk*
[b]*State Key Laboratory of Synthetic Chemistry, The Chinese University of Hong Kong, Shatin, New Territories, Hong Kong, China*

insights are crucial for the rational design of more robust, high-performance organic electronic materials.

While recent reviews have separately covered organic radicals and organic ions, they have not comprehensively addressed π-conjugated radical cations. Reviews on π-conjugated radicals have predominantly focused on neutral species,[13,14,18–21] while those on hydrocarbon-based cations have overlooked their radical character.[22] This review fills this gap by providing a comprehensive overview of fully characterized π-conjugated radical cations, with a particular emphasis on structures resolved by single-crystal X-ray crystallography. We examine key structural motifs that impart stability and highlight their applications in organic electronics. Finally, we assess the current state of the field and suggest future research directions. To systematically organize this body of work, we classify the discussed radical cations into three categories. Mono-radical cations refer to species containing a single unpaired electron and a single positive charge. Multiple radical cations are those that possess more than one unpaired electron and/or carry more than a single positive charge. Fractional radical cations describe systems in which the unpaired electrons and/or positive charges are shared by multiple π-conjugated molecules, resulting in a non-integer (fractional) distribution of spin or charge per molecule. In each category, π-conjugated radical cations are grouped according to the stabilization strategies employed.

2. Mono-radical cations

This section classifies mono-radical cations into three groups based on their structural features. When a mono-radical cation exhibits more than one such feature—for example, containing both a nitrogen and a sulfur atom—the structural element that contributes more significantly to the stabilization of the radical cation takes precedence in classification. Only in rare cases are radical cations with different structural features discussed together, as their conjugated backbones are closely related.

2.1 Conjugated hydrocarbons

Radical cations of conjugated hydrocarbons are usually stabilized by two strategies: steric protection and delocalization of spin density and charge. Steric protection involves introducing bulky substituents to kinetically protect the radical cation from dimerization or nucleophilic attacks, albeit at the cost of hindering or even blocking π–π interactions. Bulky groups employed in the reported radical cations of polycyclic arenes include *tert*-butyl and mesityl groups as well as bicyclo[2.2.2] octene and norbornene units, as demonstrated with Fig. 2. Hexa-*peri*-hexabenzocoronene (HBC) and quaterphenyl represent fragments of graphene and poly-*p*-phenylene, respectively, and compounds **1** and **2** are their *tert*-butylated derivatives, respectively. Chemical oxidation of **1** with $Ag^{+}(Al(OC(CF_3)_3)_4)^{-}$ affords its radical cation, which forms a π-stacked dimer exhibiting short C···C distances ranging from 3.3 to 3.5 Å in the crystal of $\mathbf{1}^{\bullet+}(Al(OC(CF_3)_3)_4)^{-}$.[23] In comparison, electrochemical oxidation of **1** in the presence of tetrabutylammonium

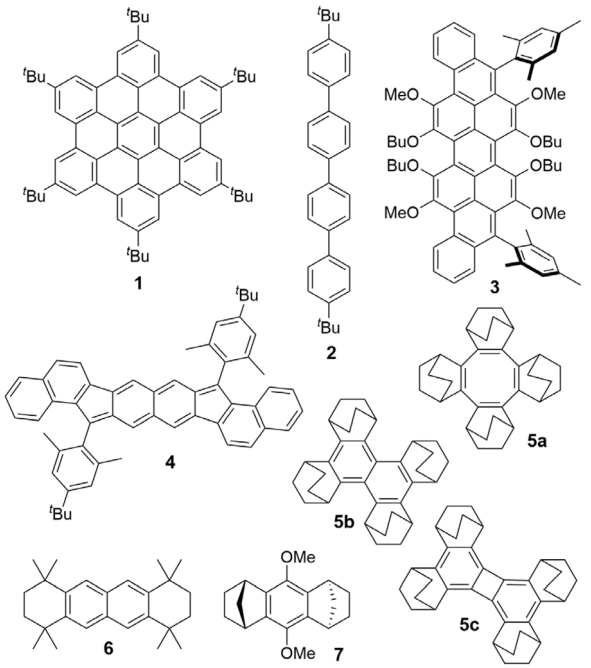

Fig. 2 Sterically protected conjugated hydrocarbons whose radical cations were fully characterized.

hexafluoroarsenate at −30 °C results in the crystal of $(\mathbf{1})_2^{\bullet+}AsF_6^{-}$, where two molecules of **1** form a π-stacked dimer.[24] Averagely, each molecule of **1** possesses half a radical and half a positive charge although bond length analysis of the crystal structure shows the two molecules in the dimer are different, suggesting the radical and positive charge are not evenly distributed among them. Oxidation of compound **2** with nitrosonium hexachloroantimonate ($NO^{+}SbCl_6^{-}$) under an argon atmosphere at −10 °C results in $\mathbf{2}^{\bullet+}$. It crystallizes from solution at −30 °C as $\mathbf{2}^{\bullet+}SbCl_6^{-}$, where two molecules of **2** also form a π-stacked dimer.[25] Notably, in the above radical cation salts, the π-stacked dimers of **1** and **2** are segregated by the counter anions or solvent molecules without further π–π interactions possibly due to steric hindrance of the bulky substituents.

The radical cations of compounds **3** [26] and **4** [27] are sterically shielded by bulky substituents: mesityl and 2,6-dimethyl-4-*tert*-butylphenyl groups, respectively. Notably, these substituents are strategically positioned on carbon atoms with the highest spin density, ensuring efficient protection of the radical centre. For dibenzoperopyrene **3**, the radical cation is further stabilized through delocalization of both positive charge and unpaired spin across the polycyclic framework. This stabilization is enhanced by global aromaticity, as evidenced by diatropic ring currents observed along the edges of the polycyclic system in the anisotropy of the induced current density (ACID) plot. As a result, the radical cation salt $\mathbf{3}^{\bullet+}SbCl_6^{-}$ exhibits high air stability in the solid state, remaining intact for at least two weeks without significant degradation. Compound **4** similarly benefits from delocalization of its unpaired spin and positive charge. Structural analysis comparing the neutral and radical

cation forms of **4** in the crystal reveals that the external naphthalene units undergo notable changes in bond lengths due to charge redistribution.

In 1993, Komatsu *et al.* demonstrated that the radical cation of cyclooctatetraene could be kinetically stabilized in its sterically congested derivative **5a** (Fig. 2), which features four fused bicyclo[2.2.2]octene units.[28] The single crystal of $\mathbf{5a}^{\bullet+}SbCl_6^-$ remains stable for several hours under ambient conditions and can be stored under refrigeration for months without decomposition. Employing the same steric protection strategy, Komatsu *et al.* later synthesized bicyclo[2.2.2]octene-fused derivatives of naphthalene (**5b** in Fig. 2), biphenylene (**5c** in Fig. 2) and anthracene. These radical cations were crystallized as hexachloroantimonate salts, which are persistent at ambient temperature even in air. Notably, crystal structural analysis of **5c** reveals that oxidation of biphenylene to its radical cation form leads to a significant shortening (by 0.042 Å) of the bonds connecting the two benzene rings, consistent with the reduction of destabilizing 4π antiaromaticity in the neutral state. Similarly, Kochi *et al.* reported compound **6**, a naphthalene derivative sterically shielded by fusing with tetramethylcyclohexane moieties.[29] The corresponding radical cation, $\mathbf{6}^{\bullet+}$, was isolated as $\mathbf{6}^{\bullet+}SbCl_6^-$ crystals. Interestingly, cocrystallization of $\mathbf{6}^{\bullet+}SbCl_6^-$ with unsubstituted naphthalene (naph) in CH_2Cl_2 solution afforded dark-green crystals of $(\mathbf{6}^{\bullet+})_2(naph)(SbCl_6^-)_2$, which are stable in air at room temperature for several days. In this crystal, two $\mathbf{6}^{\bullet+}$ cations sandwich a neutral naphthalene molecule, forming a diradical dicationic (hetero)trimer in which the central naphthalene is rotated by 90° relative to the radical cations. Bond length analysis suggests that negative charge is transferred from naphthalene to $\mathbf{6}^{\bullet+}$, which in turn is not a true mono radical cation. Likewise, Ishihara *et al.* used norbornene units to sterically protect the radical cation of *p*-dimethoxybenzene in compound **7**.[30] Oxidation of **7** by $FeCl_3$ produces a persistent radical cation, which crystallizes as $\mathbf{7}^{\bullet+}FeCl_4^-$. This result confirms that single-electron oxidation of arenes to yield radical cations is achievable under typical Scholl reaction conditions, providing evidence to support the radical cation mechanism for Scholl reactions.[31]

The unpaired spin and positive charge in radical cations of conjugated hydrocarbons can be effectively delocalized by π-systems such as phenalenyl, Thiele's hydrocarbon, and azulene. As shown in Fig. 3a, phenalenyl delocalizes a radical or a positive charge across seven carbon atoms *via* resonance. Leveraging this capability, Kubo *et al.* designed and synthesized acetylene-linked bisphenalenyl **8**,[32] which resonates with a closed-shell cumulene structure (Fig. 3b). Compound **8** exhibits biradical character, confirmed experimentally and theoretically. It reacts with 2,3,5,6-tetrafluorotetracyanoquinodimethane (F_4-TCNQ) to form a charge–transfer complex, $\mathbf{8}^{\bullet+}(F_4\text{-TCNQ})^-$, with complete charge transfer, as determined by Raman spectroscopy. This crystal remains stable in ambient conditions for weeks and shows a conductivity of 1.43 S cm^{-1} at 280 K owning to efficient π–π overlap in a π-stacked one-dimensional chain with a staggered packing motif. Notably, cooling $\mathbf{8}^{\bullet+}(F_4\text{-TCNQ})^-$ to 90 K induces formation of a C–C σ bond between a F_4-TCNQ's $C(CN)_2$ group and

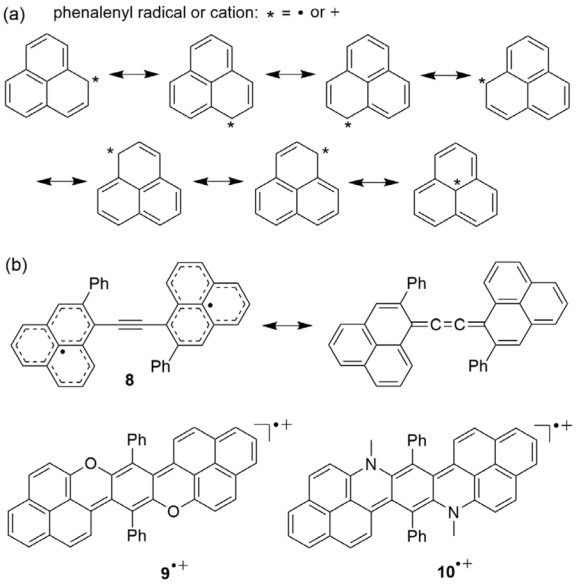

Fig. 3 (a) Resonance structures of phenalenyl radical or cation; (b) bisphenalenyls **8**–**10**.

a phenalenyl carbon. Unlike **8**, *O*- and *N*-substituted bisphenalenyls (**9** and **10**, respectively)[12,33] feature quinoid-linked phenalenyl units shown in Fig. 3b and were synthesized in radical cation form *via* reduction of their dications. Their triflate salts, $\mathbf{9}^{\bullet+}(SO_3CF_3)^-$ and $\mathbf{10}^{\bullet+}(SO_3CF_3)^-$, exhibit π-stacking between phenalenyl units with intermolecular C···C contacts as short as 3.07 Å for **9**. DFT calculations link these intermolecular closer-than-van-de-Waals contacts to intermolecular spin–spin coupling. Single crystals of $\mathbf{9}^{\bullet+}(SO_3CF_3)^-$ and $\mathbf{10}^{\bullet+}(SO_3CF_3)^-$ exhibit room-temperature conductivities of 1.31×10^{-2} S cm^{-1} and 1.16×10^{-2} S cm^{-1}, respectively. In addition, thin films of $\mathbf{10}^{\bullet+}(SO_3CF_3)^-$ function as ambipolar semiconductors with hole and electron mobilities on the order of 10^{-5} cm^2 V^{-1} s^{-1}.

As shown in Fig. 4a, the radical cation of Thiele's hydrocarbon (TH) is stabilized by the formation of a central benzene ring. Such aromaticity-enhanced stabilization has been used to develop stable conjugated radical cations based on TH (shown in blue), as demonstrated by compounds **11**–**13** in Fig. 4b. Bunz *et al.* found that the radical cations of *N*,*N*′-diarylated dihydrodiazapentacene **11a**/**b** remained stable in CH_2Cl_2 for 24 h under ambient condition.[34] In the crystal structure of $\mathbf{11a}^{\bullet+}SbF_6^-$, the centre ring and adjacent nitrogen-embedded six-membered ring have less bond length alternation than the neutral form, indicating increased aromaticity in these rings, which is also supported by nucleus-independent chemical shift (NICS) calculation. Such an increase in aromaticity can explain the observed high stability of the radical cation of **11a**/**b**. For the same reason, the radical cation of compound **12** exhibits similar stability as its *N*-substituted analogue (**11a**/**b**). Its salt $\mathbf{12}^{\bullet+}SbF_6^-$ in CH_2Cl_2 solution showed negligible spectral change after one day under aerated conditions at room temperature.[35] Compound **13** is similar to **12** by containing oxygen-incorporated TH in spite of extra carbonyl groups in the π-backbone.[36] The radical cation of **13** is thermodynamically

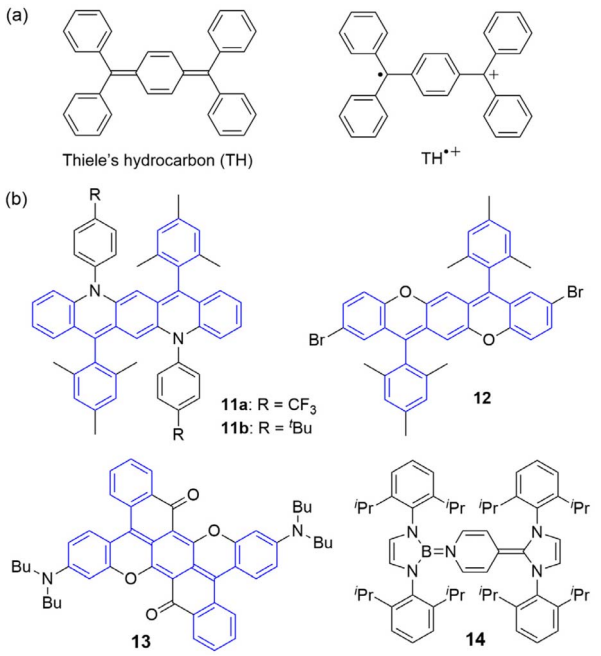

Fig. 4 (a) Thiele's hydrocarbon (TH) and its radical cation; (b) compounds derived from TH (**11**–**13**) and a BN analogue of TH (**14**).

stabilized by delocalizing its unpaired spin across the whole molecule including aniline nitrogen and benzoyl carbon atoms. As a result, $\mathbf{13}^{\bullet+}SbF_6^-$ is very stable in solid state with no degradation after 10 months and in CH_2Cl_2 solution with no degradation after 7 days under ambient conditions and room light. Spin-coated films of neutral **13** function as a p-type semiconductor with field-effect mobility of 1.3×10^{-5} cm^2 V^{-1} s^{-1}, while spin-coated films of $\mathbf{13}^{\bullet+}DDQ^-$ exhibits ohmic behavior with a room-temperature conductivity of 7.7×10^{-3} S cm^{-1}. Having two C atoms replaced by B and N atoms, respectively, compounds **14** is a B–N analogue of TH.[37] Oxidation of **14** with $Ag^+SbF_6^-$ results in $\mathbf{14}^{\bullet+}SbF_6^-$, which represents a rare example of an isolable boron-containing radical cation.

A seven-membered carbocycle capable of forming an aromatic tropylium cation has also been employed as a structural motif to stabilize radical cations, as exemplified by compounds **15** and **16** (Fig. 5).[38] DFT calculations revealed that upon one-electron oxidation, the seven-membered ring in $\mathbf{15}^{\bullet+}$ becomes more positively charged compared to neutral **15**, while the unpaired spin is delocalized across the framework, with higher density localized on the seven-membered ring and the inner rim of the five-membered rings, the latter being shielded

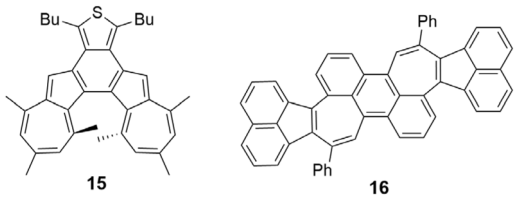

Fig. 5 π-Systems containing seven-membered carbocycles.

by the helical conformation of $\mathbf{15}^{\bullet+}$. Stepwise chemical oxidation of **16** with $NO^+SbF_6^-$ generated the radical cation ($\mathbf{16}^{\bullet+}$) and the dication ($\mathbf{16}^{2+}$), which were isolated as their hexafluoroantimonate salts.[39] DFT calculations indicate that in $\mathbf{16}^{\bullet+}$, the spin is delocalized across the π-backbone, with higher density on the seven-membered rings, while in $\mathbf{16}^{2+}$, the positive charges are predominantly located on the seven-membered carbocycles. In the single crystal of $\mathbf{16}^{\bullet+}SbF_6^-$, $\mathbf{16}^{\bullet+}$ adopts a cisoid conformation, and packs into a cofacial π-dimer. Partial oxidation with $NO^+SbF_6^-$ can yield fractional radical cation salt. Interestingly, partial oxidation of **16** with $NO^+SbF_6^-$ resulted in crystals of a mixed-valence species $\mathbf{16}\cdot(\mathbf{16}^{\bullet+})_3$ consisting of one-quarter equivalent of the neutral molecule and three-quarters equivalent of the radical cation. The crystal structure of this mixed-valence species features a huge trigonal unit cell that contains 72 molecules of **16**, 54 SbF_6^- counter anions and 101 disordered hexane molecules.

Double helicenes were recently been demonstrated by Miao and coworkers to be an effective structural motif for stabilizing radical cations. Chemical oxidation of double [5]helicene **17a/b** (Fig. 6) yielded a robust radical cation, showing negligible spectral changes after its CH_2Cl_2 solution was exposed to ambient air in the dark for 60 days.[40] Such a high stability is attributed to spin delocalization in the π-backbone and the twisted structure impeding dimerization. Notably, crystal structures of neutral **17a** and radical cation salt $\mathbf{17a}^{\bullet+}PF_6^-$ exhibit nearly identical π–π stacking, with PF_6^- occupying the site of CH_2Cl_2 in the neutral crystal. Dip-coated films of $\mathbf{17a}^{\bullet+}PF_6^-$ showed conductivity up to 1.32 ± 0.04 S cm^{-1}, while **17a** behaved as a p-type semiconductor with mobility of 0.064 ± 0.003 cm^2 V^{-1} s^{-1}. Moreover, photochemical oxidation of **17b** in

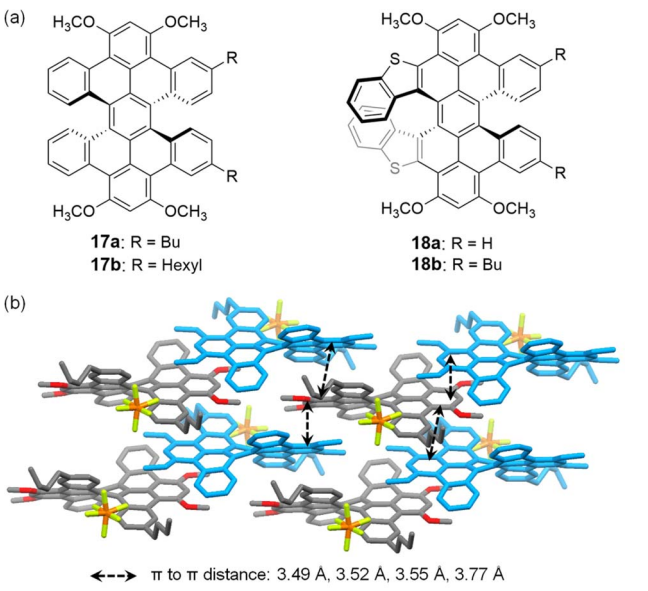

Fig. 6 (a) Double helicenes **17a/b** and **18a/b**; (b) π–π stacking in the crystal of $\mathbf{17a}^{\bullet+}PF_6^-$, where the (*M*, *M*) enantiomer is shown in blue, and the (*P*, *P*) enantiomer is colored according to the elements. Reproduced with permission from ref. 40. Copyright 2022 American Chemical Society.

the solid state with O_2 generated its radical cation, enabling OFETs to function as nonvolatile optoelectronic memory with switching contrast above 10^3 and long-term stability. Similarly, S-containing double helicenes **18a/b** (Fig. 6) formed robust radical cations. **18a**$^{\bullet+}$ remained stable in CH_2Cl_2 under ambient air in the absence of light for four weeks and retained ~85% absorption in water-saturated CH_2Cl_2 after 8 days.[41] The salt **18b**$^{\bullet+}SbF_6^-$ achieved a conductivity of 0.16 S cm^{-1} at room temperature, due to strong π–π interactions in its crystal structure.

2.2 Nitrogen-containing systems

Stable radical cations often feature heteroatoms that act as spin-bearing sites,[42] and tertiary arylamines have long been used to develop radical cation species. For example, *N*,*N*,*N*′,*N*′-tetramethyl-*p*-phenylenediamine (Fig. 7), can be readily converted by one-electron oxidation into a stable semiquinone radical, known as Wurster's blue.[43] Another example is tris(4-bromophenyl)ammoniumyl hexachloroantimonate, which is commonly known as magic blue (Fig. 7) and used as a popular oxidizing agent in organic and organometallic chemistry.

Triphenylamine radical cations lacking *para* substituents are inherently unstable due to high spin densities at para positions.[44] Stabilization can be achieved by *ortho*-bridging aryl groups, as seen in triarylamines **19–23** (Fig. 8), which enhance planarity of π-frameworks and delocalize spin density. Crystal structures reveal that neutral trioxytriphenylamine **19** is shaped like a shallow bowl with a sp^3-hybridized central N atom, whereas its radical cation is flat with shorter C–N bonds.[45] The delocalization of unpaired spin across the π-framework of **19**$^{\bullet+}$, including oxygen atoms, prevents dimerization or oxygenation under ambient conditions. Similarly, the radical cations of S,C,C-bridged triarylamine **20**[46] and O,C,C-bridged triarylamines **21a/b**[47] all exhibited appreciable stability, with the absorption spectra of their CH_2Cl_2 solutions remaining virtually unchanged after one day and the crystals of their hexachloroantimonate salts being stable under ambient conditions. In the crystals, the π-frameworks of **20**$^{\bullet+}$ and **21a**$^{\bullet+}$ are essentially flat while that of **21b**$^{\bullet+}$ is slightly twisted. DFT calculations indicate spin delocalization across all three radicals, with the highest density on the central nitrogen. Notably, sulfur in **20**$^{\bullet+}$ shares more spin density than oxygen in **21a**$^{\bullet+}$ and **21b**$^{\bullet+}$. Spin density on the central N atom increases in the order of **20**$^{\bullet+}$ (+0.294) < **21a**$^{\bullet+}$ (+0.328) < **21b**$^{\bullet+}$ (+0.332), while Mulliken charges on it decrease in the order of **20**$^{\bullet+}$ (+0.345) > **21a**$^{\bullet+}$ (+0.290) > **21b**$^{\bullet+}$ (+0.194).

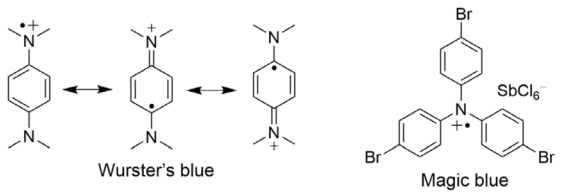

Fig. 7 Resonance structure of Wurster's blue and structure of magic blue.

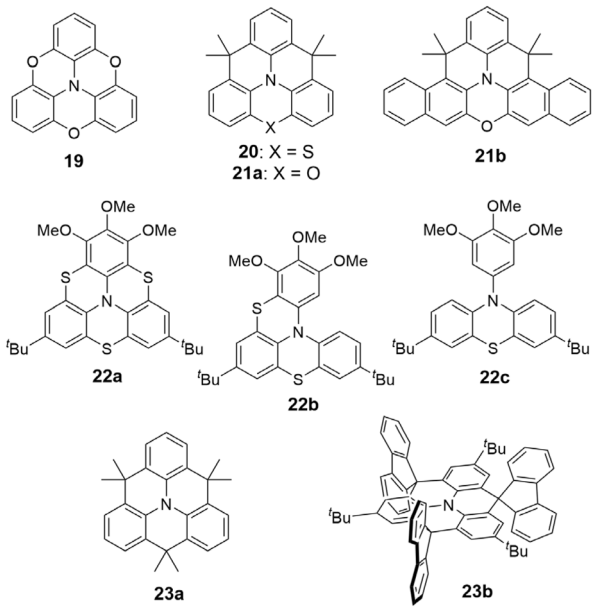

Fig. 8 Structures of triarylamines **19–23**.

Very recently, Kivala *et al.* synthesized trithiatriphenylamine **22a** (Fig. 8) and compared it to **22b/c** (Fig. 8) with fewer thia bridges.[48] The radical cation of **22a**, in the form of **22a**$^{\bullet+}SbCl_6^-$, remained stable for months under ambient conditions, showing no degradation in $CHCl_2CHCl_2$ solution. In contrast, **22b**$^{\bullet+}$ and **22c**$^{\bullet+}$ exhibited significantly lower stabilities, with half-lives of 1.06 and 6.04 days, respectively, in tetrachloroethane at 80 °C under inert atmosphere. Spin delocalization differences explain this stability: the spin density of **22a**$^{\bullet+}$ is delocalized across the whole molecule while that of **22b**$^{\bullet+}$ is mostly distributed over the methoxylated phenothiazine subunit and that of **22c**$^{\bullet+}$ is localized on the phenothiazine ring. The crystal structure of **22a**$^{\bullet+}SbCl_6^-$ exhibits a planarized π-backbone relative to the saddle-shaped neutral molecule and one-dimensional stacking of **22a**$^{\bullet+}$. Additionally, **22a** forms charge-transfer complexes with 7,7,8,8-tetracyanoquinodimethane (TCNQ) or F_4-TCNQ, transferring 0.29 e$^-$ and 0.42 e$^-$ to TCNQ in the 1 : 1 and 2 : 1 complexes, respectively, or 0.90 e$^-$ to F_4-TCNQ in the 1 : 1 complex, as determined from anion bond lengths. In these crystals, molecules of **22a** and TCNQ or F_4-TCNQ stack in a column with an alternative arrangement. However, the electrical conductivities of these charge transfer complexes as well as **22a**$^{\bullet+}SbCl_6^-$ were not reported.

Compound **23a**, a sp^3 hybridized carbon-bridged triphenylamine, is oxidized by Ag^+ to it radical cation, which is isolated in the form of **23a**$^{\bullet+}(Al(OC(CF_3)_3)_4)^-$ and characterized by X-ray crystallography.[49] Similar to **19**$^{\bullet+}$, the polycyclic framework of **23a**$^{\bullet+}$ adopts a planar conformation, in contrast to the shallow bowl-shaped geometry of neutral **23a**. DFT calculations indicate that the central N atom in **23a**$^{\bullet+}$ carries a higher spin density (+0.366) compared to **19**$^{\bullet+}$ (+0.328), indicating greater localization of the unpaired electron. When oxidized with 0.5 equivalent of $Ag^+(Al(OC(CF_3)_3)_4)^-$, **23a** forms

a dimerized product, suggesting the reactivity of **23a**$^{\bullet+}$. Compound **23b**, a sterically protected triphenylamine derivative of **23a**, incorporates spiro-fluorene moieties perpendicular to the planar triphenylamine core and *tert*-butyl groups at para positions.[50] Its radical cation remains stable in CH_2Cl_2 solution for months at 7 °C under N_2 and in solid form under ambient conditions for weeks.

Incorporating *ortho*-bridged triphenylamine into a double helicene structure provides additional kinetic protection for its radical cation through helical curvature around the spin centre, as demonstrated in compounds **24–26** (Fig. 9). The radical cations of **24** and **25** were crystallized as **24**$^{\bullet+}SbCl_6^-$ and **25**$^{\bullet+}NTf_2^-$, respectively.[51,52] Crystal structures reveal that oxidation induces planarization in both molecules, accompanied by shortened helical pitches in their radical cation states. Notably, the absorption spectrum of **24**$^{\bullet+}SbCl_6^-$ in CH_2Cl_2 solution remained unchanged for 2 weeks under ambient air and room light, whereas **25**$^{\bullet+}NTf_2^-$ retained its spectral profile for 1 day under an inert atmosphere. Compound **26**, a double hetero[5]helicene synthesized *via* oxidative dimerization of benzo[*b*]phenoxazine,[53] forms stable radical cations in both racemic and enantiopure forms with different counteranions, which influence the molecular packing in the resulting radical cation salts.[54] Racemic and enantiopure **26**$^{\bullet+}NTf_2^-$ exhibit one-dimensional π–π stacking with counteranions intercalated between stacks, though enantiomers in the racemic crystal are separated by a larger π–π distance. In contrast, in the racemic and enantiopure **26**$^{\bullet+}SbCl_6^-$ crystals, the interactions between **26**$^{\bullet+}$ and $SbCl_6^-$ prevent continuous π–π stacking of **26**$^{\bullet+}$ likely due to the matching between the curvature of **26**$^{\bullet+}$ and the spherical shape of the $SbCl_6^-$ anion. Despite the close π–π stacking, racemic and enantiopure crystals **26**$^{\bullet+}NTf_2^-$ exhibited low conductivity of 1.22×10^{-8} S cm^{-1} and 2.86×10^{-8} S cm^{-1}, respectively. For comparison, vacuum-deposited films of neutral **26** behaved as a p-type semiconductor with a field effect mobility of 2×10^{-5} cm^2 V^{-1} s^{-1}.[53] Incorporating triphenylamine into a larger curved π-scaffold yields phenylenediamine-linked nanographene **27** (Fig. 9) whose radical cation remains stable in CH_2Cl_2 solution for 8 days under ambient conditions without degradation.[55] Interestingly, **27** adopts a Z-shaped *anti* conformation in its neutral state, whereas its radical cation assumes a C-shaped *syn* conformation in the **27**$^{\bullet+}SbF_6^-$ crystal. The stability of **27**$^{\bullet+}$ can be attributed to contribution from quinoidal resonance in **27**$^{\bullet+}$ and kinetic protection from the curved π-scaffold.

N,*N*′-Disubstituted dihydrodiazaacenes, such as compounds **28a–c** [56] (Fig. 10), serve as general π-scaffolds to stabilize radical cations because one-electron oxidation transforms their central dihydropyrazine ring from antiaromatic to non-aromatic or weakly aromatic, as evidenced by DFT-calculated NICS values. This stabilization mechanism also applies to the radical cation of compound **29** (Fig. 10).[57] Consequently, the radical cations of **28a–c** and **29** exhibit comparable stability with their absorption spectra essentially unchanged under ambient conditions for at least 24 h. Crystal structures reveal that the diazaacene backbones of **28a–c** are flat in both neutral and radical cations forms, while the dibenzo[*a*,*c*]phenazine backbone of **29** changes from a V-shaped conformation in the neutral state to a twisted conformation in the radical cation, with the dihydropyrazine ring flattened. Notably, the formation of stable radical cation of **28a** is related to the doping of p-type semiconductors based on *N*,*N*′-disubstituted dihydrodiazapentacenes.[58,59]

Based on the radical cation of *N*,*N*′-disubstituted dihydrophenazine, Wang *et al.* developed a water-soluble bissulfonate salt **30** (Fig. 10).[60] The radical cation in **30** resists dimerization and disproportionation, attributable to intermolecular coulombic repulsion and steric hindrance from sulfonate groups. It also has an appropriate electron density to avoid reactions with oxygen or water. As a result, **30** exhibits

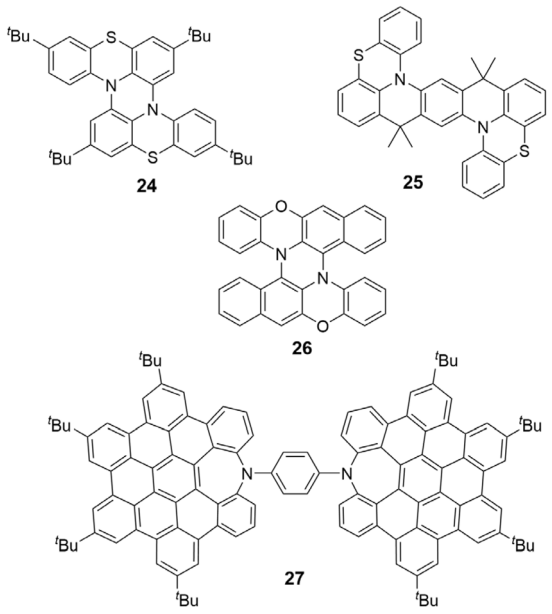

Fig. 9 Triarylamine-incorporated double helicenes **24–26** and phenylenediamine-linked nanographene **27**.

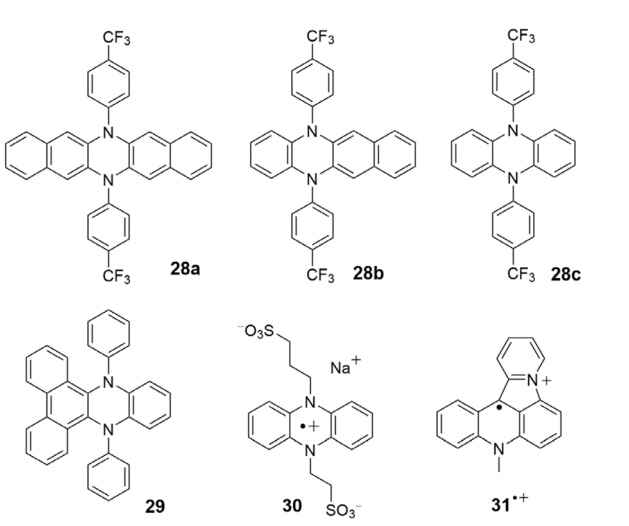

Fig. 10 *N*,*N*′-Disubstituted-dihydrodiazaacenes **28a–c** and related structures.

remarkable stability, with no decomposition observed in aqueous solution under ambient conditions for more than 70 days (monitored by UV-Vis spectroscopy). Aqueous organic redox flow batteries using **30** as the posolyte and $ZnCl_2$ as the negolyte demonstrated extremely stable performance over 2500 cycles (~27 days). Radical cation **31**$^{\bullet+}$ (Fig. 10), also known as viridium,[61] features a structure related to *N*,*N*′-disubstituted dihydrophenazine. It exhibits exceptional thermodynamic stability in solution under ambient conditions, as confirmed by Electron Paramagnetic Resonance (EPR) and UV-Vis spectroscopy over two months, due to full spin delocalization across its π-backbone. In the solid state, **31**$^{\bullet+}$ arranges into one-dimensional columns with a π–π distance of 3.29 Å. In aqueous or perfluorohydrocarbon solutions, it forms π-stacked dimers.

As an electron-rich aromatic heterocycle prone to oxidation, pyrrole serves as a building block for π-conjugated radical cations. While *N*-annulated rylenes formally incorporate fused pyrrole units, their radical cations are not further discussed here because their spin density and singly occupied molecular orbitals are delocalized across the rylene backbone but located minimally on the nitrogen atoms.[62] Pyrrole-containing multiple cations are discussed in the next session. *N*,*N*′-Diarylated tetrabenzotetraaza[8]circulene **32a/b** (Fig. 11) yields highly stable radical cations upon chemical oxidation.[63] This stability is highlighted by the 83% yield of **32a**$^{\bullet+}$ obtained after aqueous work-up, CH_2Cl_2 extraction, and silica gel column chromatography under ambient conditions. The stability arises from delocalization of spin density across the tetrabenzotetraaza[8]circulene backbone, with the highest spin density localized on the α-carbons of the *N*-octylated pyrrole units. In their hexachloroantimonate salt crystals, **32a**$^{\bullet+}$ and **32b**$^{\bullet+}$ both exhibit planar structures but adopt distinct stacking arrangements: **32a**$^{\bullet+}$ forms eclipsed stacking with an intermolecular π–π distance of 3.32 Å, whereas **32b**$^{\bullet+}$ adopts a slip-stacked arrangement. Pyrrole-embedded buckybowl **33a** and its planar analogue **33b** generate radical cations of different reactivities in solution.[64] Despite similar spin delocalization across the π-backbones with higher spin density localized on pyrrole carbons, the reactivity divergence arises from the strain induced by the positive curvature of **33a**. In both single crystals and low temperature solution states, **33a**$^{\bullet+}$ undergoes reversible σ-dimerization between the internal pyrrole α-carbons, whereas **33b**$^{\bullet+}$ selectively forms a π-dimer with a short π–π distance of 3.14 Å.

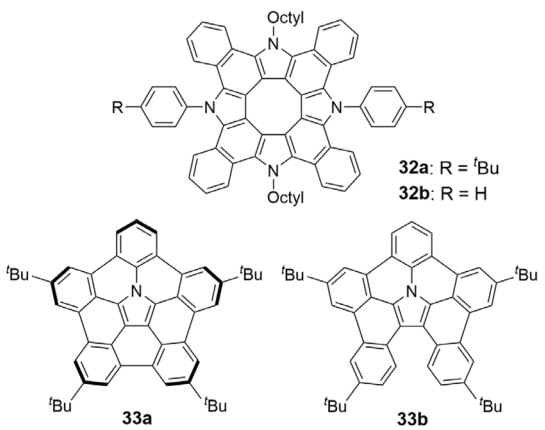

Fig. 11 Pyrrole-embedded molecules **32** and **33**.

2.3 Sulfur-containing systems

Sulfur-containing π-conjugated radical cations often feature sulfur atoms in thiophene or tetrathiafulvalene (TTF) units, as exemplified by the molecules shown in Fig. 12a and b, respectively. The radical cations of bithiophene and terthiophene are sterically protected in their bicyclo[2.2.2]octene-fused derivatives **34** and **35a** (Fig. 12a),[65] similar to the sterically congested hydrocarbons **5** and **6** (Fig. 2). Such kinetical stabilization allows the crystals of **34**$^{\bullet+}SbF_6^-$ and **35a**$^{\bullet+}SbF_6^-$ to be stable without decomposition after the crystals were left to stand at room temperature under air for one month. The structure of **35**$^{\bullet+}$ involves a significant contribution from the quinoidal resonance as indicated by crystal structure and ESR measurement as well as theoretical calculations. Notably, oxidation of sterically protected bithiophene and terthiophene (**34** and **35**) with $NO^+SbF_6^-$ yields radical cations, whereas longer oligothiophenes under the same conditions form dications. Without a bicyclo[2.2.2]octene moiety at the centre thiophene ring, **35b**$^{\bullet+}$ forms π-dimer with intermolecular distance as short as 2.976 Å between the beta carbon atoms of the central thiophene units.[66] Compound **36** is a macrocycle composed of four ethynylene-thienylene and two vinylene-thienylene units, whose radical cation remains stable in solid state but degrades in CH_2Cl_2 solution under ambient condition.[67] In the crystal of **36**$^{\bullet+}SbF_6^-$, **36**$^{\bullet+}$ forms a π-dimer, (**36**$^{\bullet+}$)$_2$, with intermolecular

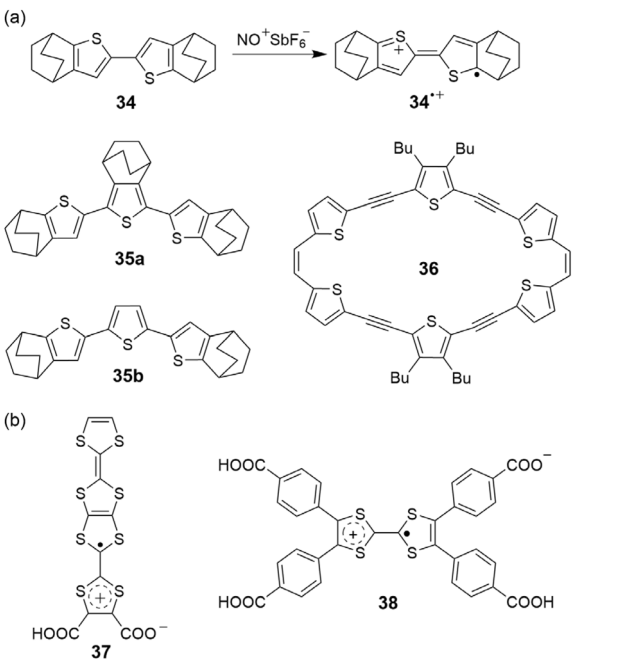

Fig. 12 (a) Thiophene-containing molecules; (b) TTF-containing zwitterions.

S···S distances of 3.7–3.8 Å comparable to twice the standard van der Waals radius of sulfur atom. Spin-coated films of **36** from its CS_2 solution exhibited a room temperature conductivity of 5.7×10^{-8} S cm^{-1}, but became a p-type semiconductor after annealing at 100 °C, with a lower conductivity of 9.2×10^{-11} S cm^{-1} and a field effect mobility of 1.4×10^{-4} cm^2 V^{-1} s^{-1}, suggesting formation of **36**$^{\bullet+}$ in the thin film by self-oxidation of **36** in air.[68]

Tetrathiafulvalene (TTF) is a well-established π-scaffold for stable radical cations, as its five-membered ring becomes aromatic with six π-electrons upon one-electron oxidation. A recent notable example is zwitterion **37** (Fig. 12b), which has a carboxylate anion attached to the π-conjugated radical cation core. It exhibits exceptionally high conductivity: 530 S cm^{-1} at 300 K and 1000 S cm^{-1} at 50 K.[69] DFT calculations reveal that the spin density in **37** is localized primarily on the carboxylate-connected TTF unit, balancing the negative charge of the carboxylate with the positive charge of the TTF moiety. Notably, **37** is unique among the radical cations discussed here, as its single-crystal structure has not been reported. Due to lack of single crystals, the high conductivity of **37** was measured from disordered bulk solids rather than crystalline materials. DFT calculations suggest stable dimeric structures in the solid state, featuring anti-parallel arrangements in both face-to-face and side-by-side stacking. Zwitterion **38**, with a structure closely related to **37**, form hydrogen-bonded organic frameworks (HOFs) in the solid state.[70] Tuning crystallization conditions yields two polymorphs of **38**, which exhibit room-temperature conductivities of 6.07×10^{-7} and 1.35×10^{-6} S cm^{-1}, respectively, as measured in pressed pellets of crystalline powder.

3. Multiple radical cations

Conjugated multiple radical cations, which possess more than one unpaired electron and/or carry more than a single positive charge, can in principle be created by incorporating several redox active π-units into a single framework. The structural factors that stabilize monoradical cations, discussed previously, are not reiterated here to avoid redundancy. This approach is exemplified by the diradical dication **39**$^{2(\bullet+)}$, which results from reduction of cyclobis(paraquat-*p*-phenylene) tetracation (**39**$^{4+}$),[71,72] as shown in Fig. 13. Specifically, **39**$^{2(\bullet+)}$ forms an inclusion complex with methyl viologen radical cation (**40**$^{\bullet+}$) by three-electron reduction of an equimolar mixture of **39**$^{4+}$ and **40**$^{2+}$. This spontaneous encapsulation of **40**$^{\bullet+}$ inside the cavity of **39**$^{2(\bullet+)}$ arises from favorable radical–radical interactions occurring between the three 4,4′-bipyridinium radical cations. The binding constant of this inclusion complex was determined using isothermal titration calorimetry and UV-Vis spectroscopy as $(5.0 \pm 0.6) \times 10^4$ M^{-1} and $(7.9 \pm 5.5) \times 10^4$ M^{-1}, respectively. Crystal structure shows that the bipyridinium radical cation subunits in **40**$^{\bullet+}$ and **39**$^{2(\bullet+)}$ are separated by 3.22 Å as measured from their centroids, and quantum chemistry calculations indicate partial charge transfer from the guest (**40**$^{\bullet+}$) to the host (**39**$^{2(\bullet+)}$), with calculated charges of +1.18 and +1.71, respectively. In the crystal of the complex, **39**$^{2(\bullet+)}$ arranges into one-dimensional columns with π–π distance of 3.28 Å. These π–π interactions enable the salt of **40**$^{\bullet+} \subset$ **39**$^{2(\bullet+)}$ $3PF_6^-$ to perform as a p-type semiconductor in a single-crystal field effect transistor with a hole mobility up to 0.05 cm^2 V^{-1} s^{-1}.[73] Notably, **39**$^{2(\bullet+)}$ was also crystallized alone as its hexafluorophosphate salt, where **39**$^{2(\bullet+)}$ stacks into a one-dimensional column with an even shorter π–π distance (3.12 Å), highlighting the dominance of strong radical–radical interactions in driving solid-state packing. In addition, the radical–radical interactions of **39**$^{2(\bullet+)}$ have been applied in developing rotaxanes and catenanes.[74,75]

On the basis of tetracation **39**$^{4+}$, Stoddart *et al.* further developed a hexacationic organic cage, **41**$^{6+}$, by incorporating three redox-active building blocks of 4,4′-bipyridinium dications into a triangular prism-shaped symmetry.[76] Reduction of **41**$^{6+}$ with cobaltocene results in its triradical trication **41**$^{3(\bullet+)}$, which has a doublet ground state. Its quartet state is only 0.08 kcal mol^{-1} higher in energy than the doublet, suggesting a strong intramolecular exchange coupling. **41**$^{3(\bullet+)}$ was crystallized in the form of $CH_3CN \subset$ **41**$^{3(\bullet+)}$ $3PF_6^-$, where a molecule of CH_3CN occupies the cavity of **41**$^{3(\bullet+)}$ (Fig. 13). In the crystal structure, **41**$^{3(\bullet+)}$ arranges into a hexagonal porous superstructure with interconnected one-dimensional channels. Each channel is formed by taking advantage of the strong radical-pairing interactions with a stacking distance of 3.15 Å between the bipyridinium radical cations and the π–π stacking between the phenylene units in the adjacent cages.

Incorporating several bridged triarylamines units in one molecule allows formation of multiple radical cations through oxidation. The overall radical nature of the resulting cationic species depends on the interactions between the individual radical sites. Macrocycles **42a/b** (Fig. 14) contain S-bridged triphenylamine units connected by methylene groups. **42a**$^{3(\bullet+)}$ and **42b**$^{4(\bullet+)}$ are formed by oxidation of each S-bridged triphenylamine unit to the radical cation, with spin density delocalized on each planarized phenothiazine unit.[77] They were both isolated in the form of hexafluoroantimonate salts, and **42a**$^{3(\bullet+)}$ appeared more stable than **42b**$^{4(\bullet+)}$, with its characteristic absorption barely changed after 48 h at room temperature. The capability of forming stable radical cations allow **42a** and **42b** to function as cathode materials in lithium-ion batteries with initial discharge capacities of 19.3 mA h g^{-1} and 28.7 mA h g^{-1}, respectively.

Compound **43a** comprises two sulfur and carbon-bridged triphenylamine (SCBT) units linked by a 1,8-naphthalene moiety, while **43b** contains two oxygen and carbon-bridged

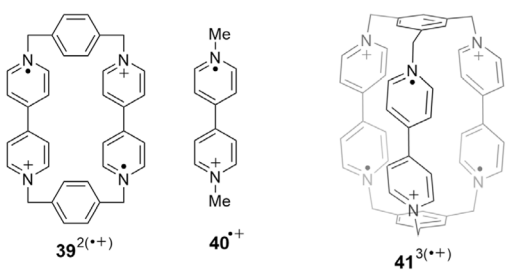

Fig. 13 Macrocyclic multiple radical cations based on 4,4′-bipyridinium.

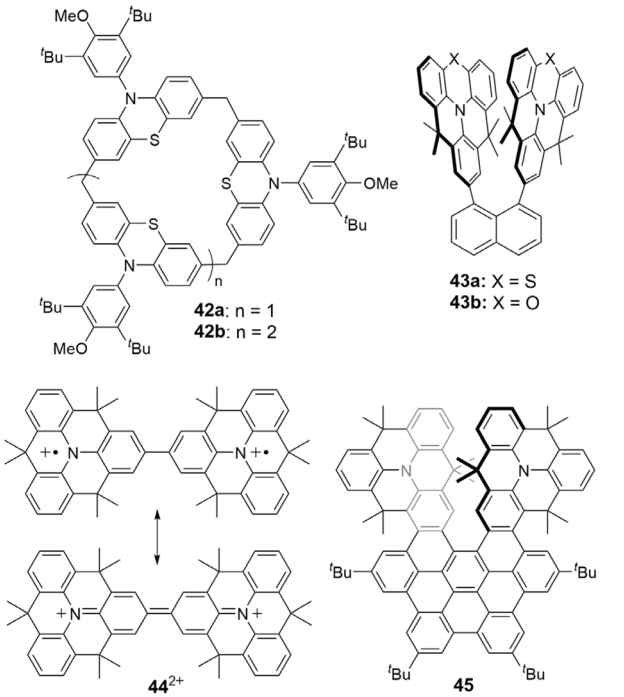

Fig. 14 Multiple triarylamine-based molecules that afford multiple radical cations.

triphenylamine (OCBT) units. Stepwise chemical oxidation of **43a** results in the radical cation and diradical dication, which were isolated in the form of **43a**$^{\bullet+}$$SbCl_6^-$ and **43a**$^{2(\bullet+)}$$2NTf_2^-$, and both species are stable under ambient conditions.[78] Single-crystal X-ray diffraction analyses revealed that both **43a**$^{\bullet+}$ and **43a**$^{2(\bullet+)}$ adopt intramolecular face-to-face close π-stacking of the SCBT units, which arises from covalent-like bonding interactions between the sulfur atoms. This is evidenced by significantly shortened S···S distances of 3.37 Å in **43a**$^{\bullet+}$ and 3.03 Å in **43a**$^{2(\bullet+)}$, both well below twice the van der Waals radius of sulfur (3.60 Å). In contrast, the crystal structures of neutral **43b**, **43b**$^{\bullet+}$$SbCl_6^-$ and **43b**$^{2(\bullet+)}$$2SbCl_6^-$ reveal that the two OCBT units progressively separate upon oxidation, with no intramolecular π–π stacking observed in the dicationic state **43b**$^{2(\bullet+)}$. In the crystal of **43a**$^{\bullet+}$$SbCl_6^-$, the SCBT units stack into a one-dimensional column, while in of **43a**$^{2(\bullet+)}$$2NTf_2^-$, the naphthalene linkers stack into one-dimensional columns, with no intermolecular overlap between SCBT units. Owing to the π–π interactions in the solid state, compressed pellets of **43a**$^{\bullet+}$$SbCl_6^-$ and **43a**$^{2(\bullet+)}$$2NTf_2^-$ exhibited room-temperature conductivity of 1.9×10^{-6} S cm^{-1} and 1.4×10^{-7} S cm^{-1}, respectively. Dication **44**$^{2+}$ has two carbon-bridged triphenylamine units linked through a C–C single bond and was obtained by oxidative dimerization of C-bridged triphenylamine **23a** (Fig. 8).[49] It has an open-shell singlet ground state, with a diradical character of 0.77. The radicals in **44**$^{2+}$ interact through resonance as shown in Fig. 14, unlike the radicals in **42a**$^{3(\bullet+)}$ and **43a**$^{2(\bullet+)}$. Compound **45** contains two C-bridged triphenylamine units bridged with a π-extended [5]helicene.[79] The dication **45**$^{2+}$ contains small contribution of open-shell singlet, with a diradical character of 0.20, which is in line with the shorter C–N bond upon oxidation, suggesting the small contribution of diradical dication character. In both **45**$^{\bullet+}$ and **45**$^{2+}$, π–π stacking are absent.

Conjugated macrocycles containing multiple triphenylamine units, such as compounds **46–48** (Fig. 15), enable stable multiple radical cations. Chemical oxidation of compounds **46a** and **46b** yields stable diradical dication that can be stored under ambient conditions.[80–82] Having 1,4-phenylene linkers, **46a**$^{2(\bullet+)}$ exhibits a triplet ground state with spins and charges delocalized over two 1,4-phenylenediamine moieties. In contrast, having 9,10-anthrylene linkers, **46b**$^{2(\bullet+)}$, exhibits a singlet ground state with spins and charges localized on two 1,3-phenylenediamine moieties, supported by shortening of the corresponding C–N bonds. In the solid state, **46a**$^{2(\bullet+)}$ arranges into a one-dimensional chain in the crystal

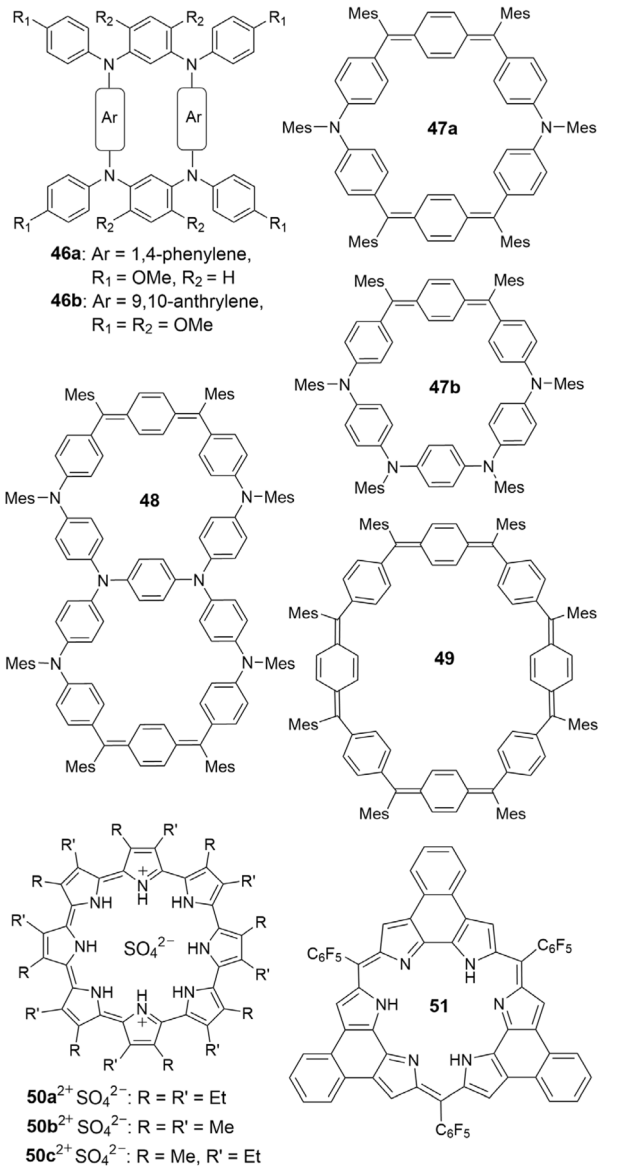

Fig. 15 Conjugated macrocycles that afford multiple radical cations.

structures of $\mathbf{46a}^{2(\bullet+)}2SbF_6^-$ and $\mathbf{46a}^{2(\bullet+)}2(Al(OC(CF_3)_3)_4)^-$, but not in the crystal structure of $\mathbf{46a}^{2(\bullet+)}2(B(C_6F_5)_4)^-$. Macrocycles **47a/b** and **48** (Fig. 15) exhibit rich redox properties, with several cationic species isolated and characterized.[83,84] $\mathbf{47a}^{2+}$ and $\mathbf{47a}^{4+}$ were both isolated as hexachloroantimonate salts. The open-shell singlet ground states of $\mathbf{47a}^{2+}$ and $\mathbf{47a}^{4+}$ exhibit diradical characters of 0.862 and 0.379, respectively, with $\mathbf{47a}^{2+}$ being globally aromatic and $\mathbf{47a}^{4+}$ globally antiaromatic. In contrast, the oxidized species of **47b** was isolated as a radical trication. Similarly, chemical oxidation of bismacrocycle **48** generates $\mathbf{48}^{2(\bullet+)}$, which possesses an open-shell singlet ground state with a high diradical character of 0.96. Similar redox behavior is observed for their hydrocarbon analogue **49** (Fig. 15).[85] $\mathbf{49}^{2+}$, isolated in the form of $\mathbf{49}^{2+}2SbF_6^-$, exhibits a globally aromatic, open-shell singlet ground state, with multiple diradical characters ($y_0 = 0.46, y_1 = 0.37, y_2 = 0.16$) calculated from the crystal structure.

Sessler *et al.* synthesized cyclo[8]pyrrole in its dicationic form, $\mathbf{50}^{2+}SO_4^{2-}$ (Fig. 15) and subsequently oxidized it to the radical trication $\mathbf{50}^{\bullet 3+}$ using I_2.[86,87] The side chains in $\mathbf{50}^{\bullet 3+}$ play a crucial role in determining the packing motifs of the radical trications in the resulting crystals. Diffusion of hexane vapor into a dichloromethane solution yielded $(\mathbf{50a}^{\bullet 3+}SO_4^{2-})_2 \cdot I_{25}^{2-} \cdot I_2$, in which $\mathbf{50a}^{\bullet 3+}SO_4^{2-}$ units form slipped π-dimers without interdimer π–π interactions. Using ethyl acetate instead of hexane resulted in $(\mathbf{50a}^{\bullet 3+}SO_4^{2-})_2 \cdot I_7^- \cdot I_{24}^-$, where two $\mathbf{50a}^{\bullet 3+}SO_4^{2-}$ units sandwich an I_7^- ion, and these sandwiches are intercalated by layers of 1D polyiodide I_{24}^- (Fig. 16a). In the crystal structure of $\mathbf{50b}^{\bullet 3+}SO_4^{2-} \cdot I_{12}^-$, the $\mathbf{50b}^{\bullet 3+}SO_4^{2-}$ units are intercalated by 1D polyiodide chains, forming a linear 1D stacked donor–acceptor structure. For $\mathbf{50c}^{\bullet 3+}SO_4^{2-} \cdot I_{16}^-$, the $\mathbf{50c}^{\bullet 3+}SO_4^{2-}$ units assemble into 2D highly ordered layers, which are intercalated with 2D polyiodide layers of I_8^- and I_{24}^-, leading to a linear 1D donor–acceptor cocrystal structure (Fig. 16b). Single-crystal of $(\mathbf{50a}^{\bullet 3+}SO_4^{2-})_2 \cdot I_7^- \cdot I_{24}^-$, $\mathbf{50b}^{\bullet 3+}SO_4^{2-} \cdot I_{12}^-$ and $\mathbf{50c}^{\bullet 3+}SO_4^{2-} \cdot I_{16}^-$ exhibited conductivity of $3.6 \pm 0.4 \times 10^{-4}$ S cm^{-1}, $7.2 \pm 0.7 \times 10^{-3}$ S cm^{-1} and $6.1 \pm 0.6 \times 10^{-1}$ S cm^{-1}, respectively, under ambient temperature. In addition, $\mathbf{50a}^{2+}SO_4^{2-}$ can transfer electrons to macrocycle **51** *via* proton-coupled electron transfer (PCET) or through an artificial electron transport chain (ETC) using I_2 as mediators and trifluoroacetic acid as proton source. This process generates the radical trication $\mathbf{50a}^{\bullet 3+}$ in the crystal $\mathbf{50a}^{\bullet 3+}SO_4^{2-}(CO_2CF_3)^-$ and the radical dication $H_3\mathbf{51}^{\bullet 2+}$ in the crystals $H_3\mathbf{51}^{\bullet 2+}2(CO_2CF_3)^- \cdot CHCl_3$ or $(H_3\mathbf{51}^{\bullet 2+})_2SO_4^{2-} \cdot 2I_3^- \cdot 2.5I_2 \cdot 6.25H_2O$.

Other notable examples of multiple radical cations include $\mathbf{52}^{(2\bullet)+}$, $\mathbf{53}^{2(\bullet+)}$ and $\mathbf{54}^{2(\bullet+)}$, as shown in Fig. 17. Azatriangulene diradical monocation $\mathbf{52}^{(2\bullet)+}$ features a polycyclic framework isoelectronic with the triangulene diradical, where a cationic sp^2-hybridized nitrogen atom replaces the central carbon atom of triangulene. Two derivatives, $\mathbf{52}^{(2\bullet)+}$, $\mathbf{53}^{2(\bullet+)}$, were isolated as $\mathbf{52a}^{(2\bullet)+}SbCl_6^-$ and $\mathbf{52b}^{(2\bullet)+}(SO_3CF_3)^-$, respectively.[88,89] They both have a triplet ground state, analogous to triangulene, with spin density delocalized along the periphery of the aza-triangulene backbone. This spin is kinetically stabilized by trichlorophenyl and mesityl substituents. As a result, $\mathbf{52b}^{(2\bullet)+}(SO_3CF_3)^-$ exhibits excellent stability, showing no changes in its absorption spectrum after 10 hours or in fluorescent intensity after 5000 seconds. Oxidation of diindinodihydrophenazine **53** with I_2 generates its diradical dication as the solid $\mathbf{53}^{2(\bullet+)}2I_3^-$, which is benchtop stable for several months under ambient conditions.[90] A large excess of reducing reagents and base is required to reduce $\mathbf{53}^{2(\bullet+)}$ back to

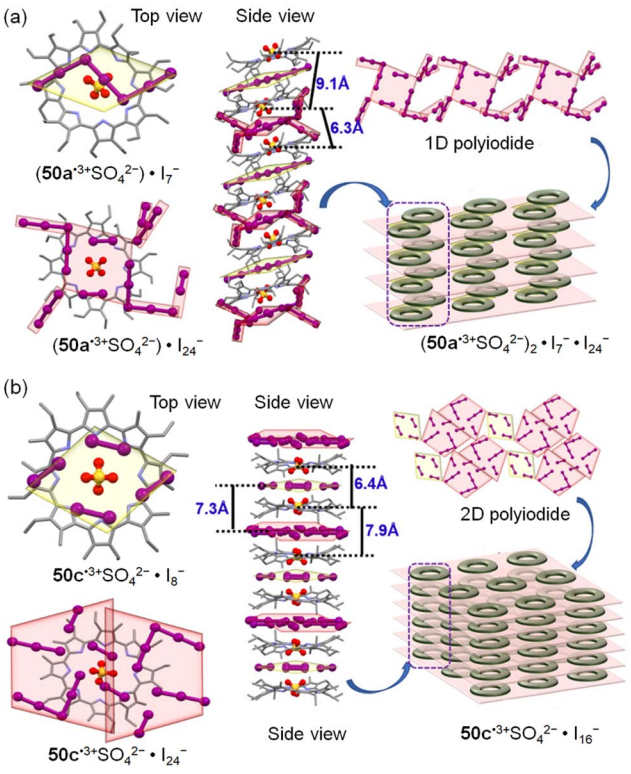

Fig. 16 Crystal structures of $(\mathbf{50a}^{\bullet 3+}SO_4^{2-})_2 \cdot I_7^- \cdot I_{24}^-$ (a) and $\mathbf{50c}^{\bullet 3+}SO_4^{2-} \cdot I_{16}^-$ (b) with cartoon representation. Reproduced with permission from ref. 86. Copyright 2025 American Chemical Society.

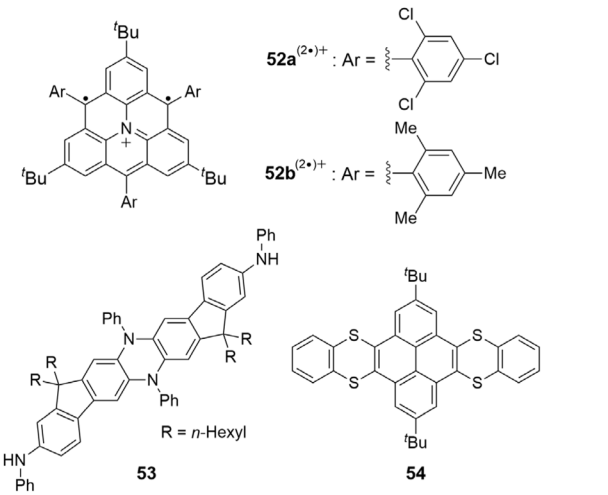

Fig. 17 Structures of cation $\mathbf{52a/b}^{(2\bullet)+}$ and compounds **53** and **54**.

53. Di(benzothiino)pyrene **54** can be stepwise oxidized to $\mathbf{54}^{\bullet+}$ and $\mathbf{54}^{2(\bullet+)}$ using 1 or 2 equivalents of $NO^{+}(Al(OC(CF_3)_3)_4)^{-}$.[91] Upon one-electron oxidation, one 1,4-dithiane ring becomes planar, with the spin density primarily localized on this ring and a concomitant contraction of the S–C bond lengths. As a result, $\mathbf{54}^{2(\bullet+)}$ adopts a fully planar backbone and possesses a triplet ground state.

4. Fractional radical cations

Fractional radical cations here refer to charged π-systems that, on average, bear non-integer charges and/or unpaired spins. These fractional charges or unpaired spins typically arise from the association of radical cations with neutral molecules in specific stoichiometric ratios, resulting in mixed-valence species. An early example is the mixed-valence salt of naphthalene (naph), reported by Fritz *et al.* in 1978.[92] In this crystal, the naphthalene radical cation $(naph)^{\bullet+}$ forms a mixed-valence dimer, $(naph)_2^{\bullet+}$, where the two crystallographically indistinguishable components are arranged in a face-to-face π-stack with an interplanar separation (3.2 Å) apparently shorter than the sum of their van der Waals radii. Polycrystalline pellets of $(naph)_2^{\bullet+}PF_6^{-}$ exhibit a room-temperature conductivity of 0.12 ± 0.046 S cm^{-1}. Mixed-valence salts, exemplified by $(naph)_2^{\bullet+}PF_6^{-}$, played a pivotal role in the development of organic conductors and superconductors.[93] Besides naphthalene, other polycyclic aromatic hydrocarbons, such as pyrene (pyr), perylene (per), triphenylene (TP) and fluoranthene (flu), form mixed-valence salts through electrocrystallization.[94–97] Single crystals of $(pyr)_{12}(AsF_6)_7$ exhibits metallic conducting behaviour in 200–300 K, and those of $(per)_2(AsF_6)_{1.1}\cdot(CH_2Cl_2)_{0.7}$ and $(per)_2(AsF_6)_{0.75}(PF_6)_{0.35}\cdot(CH_2Cl_2)_{0.85}$ exhibit very high conductivities of 1200 S cm^{-1} at 300 K and 70 000 S cm^{-1} around 285 K, respectively, owning to the 1D stacks of perylene molecules in the mixed-valence salts. In contrast, polycrystalline samples of $(TP)_2PF_6$, $(flu)_2PF_6$ exhibit low conductivity of 7×10^{-3} S cm^{-1} and 0.05 S cm^{-1} at room temperature, respectively.[98]

Tetrathiafulvalene (TTF) not only forms radical cation salts as shown in Fig. 1, but also participates in mixed-valence systems, exemplified by the TTF-TCNQ complex, the first purely organic material reported to exhibit electrical conductivity comparable to that of metals.[99] The high conductivity of TTF-TCNQ arises from its mixed-valence state, in which TTF and TCNQ carry partial charges of +0.59 and −0.59, respectively, and form segregated stacks in the solid state.[100,101] Similarly, TTF analogues and derivatives also support mixed-valence states. A prominent example is tetramethyltetraselenafulvalene (TMTSF, Fig. 17), which forms superconducting mixed-valence salts. $(TMTSF)_2^{\bullet+}PF_6^{-}$ exhibits a conductivity of 10^5 S cm^{-1} around 20 K at ambient pressure and was the first organic superconductor discovered, with a superconducting transition temperature of 0.9 K under a pressure of 12 kbar,[102] while single crystals of $(TMTSF)_2^{\bullet+}ClO_4^{-}$ transit to a superconductor below 1.4 K in the absence of applied pressure.[103]

Compound **55** (Fig. 18) can be regarded as an indenofluorene-extended tetrathiafulvalene (TTF). Oxidation of

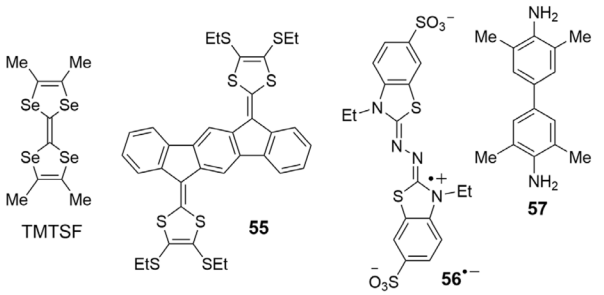

Fig. 18 Structures of TTF analogues and derivatives.

55 *via* electrocrystallization yields either the mixed-valence salt $\mathbf{55}\cdot(BF_4)_{1.5}$ or the radical cation salts $\mathbf{55}^{\bullet+}PF_6^{-}$ and $\mathbf{55}^{\bullet+}TaF_6^{-}$, depending on the electrolyte employed.[104] The mixed-valence salt contains $\mathbf{55}^{\bullet+}$ and $\mathbf{55}^{2+}$ in a 1 : 1 ratio. In the crystal structures of all three salts, the **55** cations form one-dimensional (1D) π-stacks. However, $\mathbf{55}\cdot(BF_4)_{1.5}$ exhibits a larger π–π distance (3.69 Å) than the other two salts, indicating stronger electrostatic repulsion between $\mathbf{55}^{\bullet+}$ and $\mathbf{55}^{2+}$ compared to that between $\mathbf{55}^{\bullet+}$ ions. As measured from the compressed powdered samples, at room temperature, $\mathbf{55}\cdot(BF_4)_{1.5}$, $\mathbf{55}^{\bullet+}PF_6^{-}$ and $\mathbf{55}^{\bullet+}TaF_6^{-}$ exhibit room-temperature conductivities of 1.3×10^{-3}, 3.07×10^{-2}, and 5.32×10^{-2} S cm^{-1}, respectively. All three salts behave as semiconductors, with conductivity decreasing by four to five orders of magnitude upon cooling to 77 K. Consistent with the intrinsic conductivity observed in the radical cation salts of **55**, a butylated derivative of **55** functions as a p-type organic semiconductor in single crystals transistors with a field effect mobility of 1.44 $cm^2\ V^{-1}\ s^{-1}$.[105] In contrast to the 1,3-dithiole rings in TTF connected through a C–C double bond, anion $\mathbf{56}^{\bullet-}$ (Fig. 18) features two 1,3-thiazole rings connected through conjugated nitrogen atoms and has a radical cation in its π-backbone. Adding tetramethylbenzidine (**57** in Fig. 18) to a solution of $\mathbf{56}^{\bullet-}$ led to the formation of the $\mathbf{56}\cdot\mathbf{57}_2$ complex as blue crystals.[106] Mulliken population analysis indicates an overall charge of −1.6 on **56** and +0.8 on **57**, confirming significant electron transfer from **57** to **56**. The charge–transfer complex of $\mathbf{56}\cdot\mathbf{57}_2$ effectively absorbs across the full solar spectrum, extending beyond 2500 nm, and was therefore employed as a photothermal material, achieving a photothermal conversion efficiency of 49.6%.

Compound **58** (Fig. 19), a derivative of bispyrrole-fused bisanthene, presents a rare example for radical cations exhibiting symmetry-broken intermolecular charge separation in the solid state.[107] Stepwise oxidation of **58** with $NO^{+}SbF_6^{-}$ generates $\mathbf{58}^{\bullet+}$ and $\mathbf{58}^{2+}$, distinguishable by absorption spectroscopy. DFT-calculated spin density indicates that spin is largely distributed along the periphery of $\mathbf{58}^{\bullet+}$. Interestingly, X-ray crystallography combined with DFT calculation-based Mulliken population analysis reveals that the crystal of $\mathbf{58}^{\bullet+}SbF_6^{-}$ is in fact a mixed valence complex comprising two different forms of **58**: a shallow bowl-shaped form bearing more positive charge ($\mathbf{58}^{m+}$) and an essentially flat form bearing less positive charge ($\mathbf{58}^{n+}$). In the crystal, the two forms of **58** arrange into a π-stack with the repeating sequence of $\mathbf{58}^{m+}\cdots\mathbf{58}^{n+}\cdots\mathbf{58}^{n+}\cdots\mathbf{58}^{m+}$. Upon

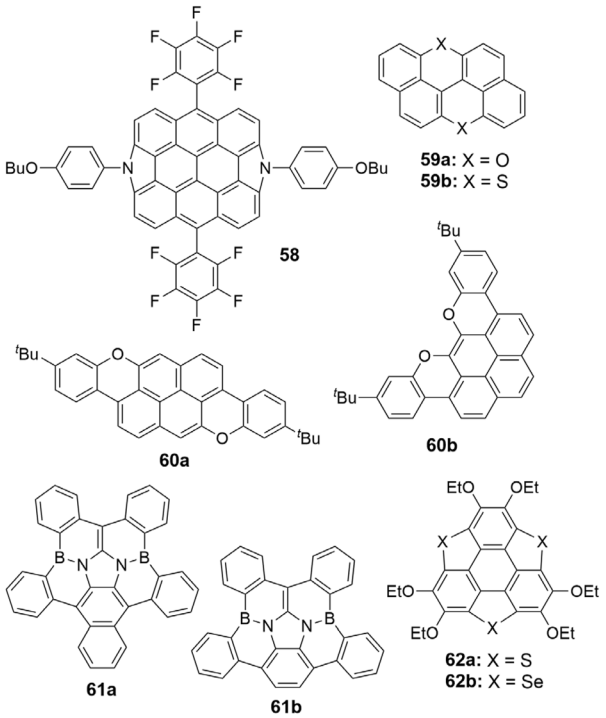

Fig. 19 Polycyclic heteroarenes that form fractional radical cations.

increasing the temperature from 173 K to 298 K, the degree of charge transfer decreases, with m decreasing from 1.4 to 1.3 and n increasing from 0.6 to 0.7. This reduced charge transfer is accompanied with a reduced bowl depth and an increased π–π distance between $\mathbf{58}^{m+}$ and $\mathbf{58}^{n+}$.

Compounds **59a** and **59b** (Fig. 19) are O and S-containing anthanthrenes, which form mixed valence salts, $\mathbf{59a}_2ClO_4$ and $\mathbf{59b}_3(ClO_4)_2$, *via* electrocrystallization.[108] In the crystals of these mixed valence salts, **59a** and **59b** molecules form 1D column, with shorter π–π distances (<3.40 Å) and greater π–π overlaps than the corresponding neutral crystals. The single crystals of $\mathbf{59a}_2ClO_4$ and $\mathbf{59b}_3(ClO_4)_2$ exhibit room temperature conductivities up to 0.11 S cm^{-1} and 0.031 S cm^{-1}, respectively. In connection with electrical conductivities of these mixed valence salts, compounds **59a** and **59b** and their derivatives in neutral forms have been applied as p-type organic semiconductors in OFETs. For example, the 3,9-diphenyl derivative of **59a** in vacuum-deposited films achieved a field effect mobility of 0.43–0.46 cm^2 V^{-1} s^{-1}, and the devices were demonstrated to be stable for five months under ambient conditions.[109]

Compounds **60a** and **60b** (Fig. 19) are a pair of regioisomeric polycyclic *O*-heteroarenes, which form mixed valence salts, $\mathbf{60a}_{10}(PF_6)_6\cdot(THF)_{16}$ and $\mathbf{60b}_3(ClO_4)_2\cdot THF\cdot(H_2O)_{0.5}$, *via* electrocrystallization.[110] In the crystals, the **60a** units assemble into a π-stacked column with an antiparallel arrangement and an average interplanar spacing of 3.33(7) Å, in contrast to the herringbone packing of neutral **60a**. Similarly, the **60b** units arrange into a π-stacked column with both pincer-like and head-to-tail packing modes and π–π distances varying from 3.21 to 3.42 Å (Fig. 20a). The crystallographically independent molecules of **60a** and **60b** within each stack display nearly identical bond lengths, indicating effective charge delocalization across the entire π-column. Two-terminal devices fabricated from a single crystal of $\mathbf{60b}_3(ClO_4)_2\cdot THF\cdot(H_2O)_{0.5}$ exhibited semiconducting behavior, demonstrated by its sigmoidal *I–V* curves and an increase in conductivity with rising temperature. The room-temperature conductivity reached values of up to 3.7×10^{-3} S cm^{-1} (ohmic) and 5.1×10^{-3} S cm^{-1} (non-ohmic).

Benzannulated B,N-doped corannulenes **61a** and **61b** (Fig. 19) undergo one-electron oxidation with $NO^+SbF_6^-$ in the presence of $NaBAr^F{}_4$ (Ar^F = 3,5-bis(trifluoromethyl)phenyl) to form mixed-valence salts $\mathbf{61a}_3{}^{2(\bullet+)}(BAr^F{}_4{}^-)_2$ and $\mathbf{61b}_3{}^{2(\bullet+)}(BAr^F{}_4{}^-)_2$. These salts exhibit high thermal stabilities under an inert atmosphere and could be stored for several weeks at room temperature.[111] In these crystals, both **61a** and **61b** exist as π-stacked trimers, $\mathbf{61a}_3{}^{2(\bullet+)}$ and $\mathbf{61b}_3{}^{2(\bullet+)}$ (Fig. 20b), with intra-trimer π–π distances of 3.28–3.29 Å and 3.34–3.35 Å, respectively. These π-stacked trimers further stack to form a column with intertrimer distances of 3.50 Å for **61a** and 3.50 Å for **61b**. EPR spectroscopy and DFT calculations indicate that $\mathbf{61a}_3{}^{2(\bullet+)}$ and $\mathbf{61b}_3{}^{2(\bullet+)}$ possess an open-shell singlet ground state, with the majority of the unpaired electrons located on the B–N bonds. As measured from the compressed pellets under

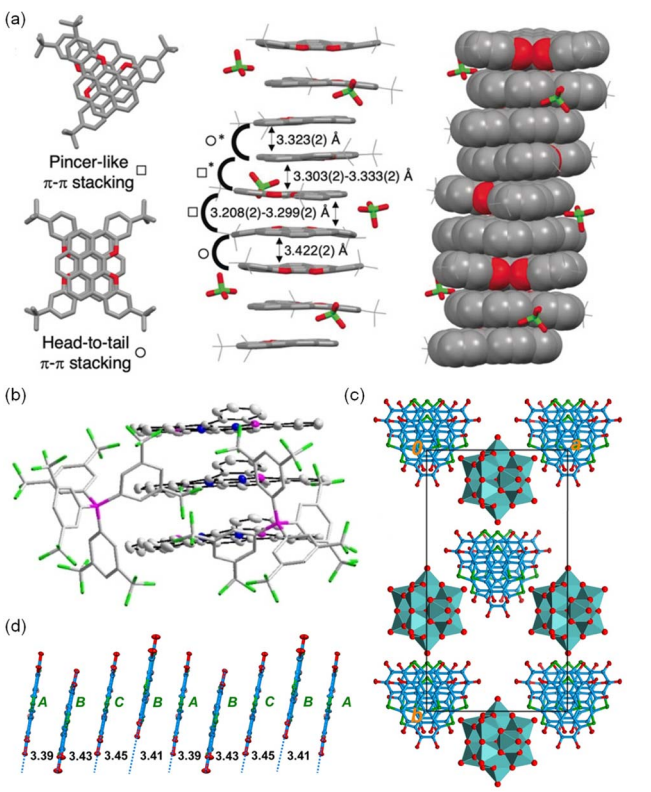

Fig. 20 (a) π–π stacking in the crystal structure of $\mathbf{60b}_3(ClO_4)_2\cdot THF\cdot(H_2O)_{0.5}$; (b) π-stacked trimer in the crystal structure of $\mathbf{61b}_3{}^{2(\bullet+)}(BAr^F{}_4{}^-)_2$; (c) a unit cell in the crystal structure of $\mathbf{62a}_4{}^{3+}(PMo_{12}O_{40})^{3-}$; (d) π–π stacking in the crystal structure of $\mathbf{62a}_4{}^{3+}(PMo_{12}O_{40})^{3-}$. Reproduced with permission from ref. 110–112. Copyright 2020, 2023 and 2024 Wiley.

a pressure of 3 MPa, $\mathbf{61a}_3^{2(\bullet+)}$ and $\mathbf{61b}_3^{2(\bullet+)}$ exhibit low conductivity of 2.48 × 10^{-7} S cm^{-1} and 3.44 × 10^{-7} S cm^{-1}, respectively.

Trithiasumanene **62a** and triselenasumanene **62b** (Fig. 19) form four mixed-valence salts *via* electrocrystallization: $\mathbf{62a}_5^{3+}(BAr^F{}_4^-)_3$, $\mathbf{62b}_5^{3+}(BAr^F{}_4^-)_3$, $\mathbf{62a}_4^{3+}(PMo_{12}O_{40})^{3-}$ and $\mathbf{62b}_4^{3+}(PMo_{12}O_{40})^{3-}$ (Ar^F = 3,5-bis(trifluoromethyl)phenyl).[112] In the $BAr^F{}_4^-$ salts, the $BAr^F{}_4^-$ anions organize into hexagonal channels that accommodate 1D π-stacked columns of $\mathbf{62a}_5^{3+}$ or $\mathbf{62b}_5^{3+}$. The crystal structure of $\mathbf{62a}_5^{3+}(BAr^F{}_4^-)_3$ contains 10 crystallographically independent **62a** molecules, each adopting a shallow bowl-shaped conformation with bowl depths ranging from 0.51 to 0.73 Å and Mulliken charges varying from +0.24 to +1.10. These units pack in a convex–concave arrangement with an average π–π distance of 3.52 Å. The crystal structure of $\mathbf{62b}_5^{3+}(BAr^F{}_4^-)_3$ contains 5 crystallographically independent molecules of **62b**, which are all nearly flat and have Mulliken charges varying from +0.41 to +1.0. In the crystal structure of $\mathbf{62a}_4^{3+}(PMo_{12}O_{40})^{3-}$ (Fig. 20c), three crystallographically independent **62a** molecules (labeled A, B, and C in Fig. 20d) adopt a flat π-framework with Mulliken charges of +0.99, +0.65, and +0.71, respectively. They assemble into π-stacked columns with a repeating ···A–B–C–B··· pattern and an average interplanar distance of 3.42 Å. Temperature-dependent electrical conductivity, measured on single crystals using a four-probe method, indicates that all four salts behave as semiconductors with thermally activated conductivity. $\mathbf{62b}_4^{3+}(PMo_{12}O_{40})^{3-}$ exhibit room temperature conductivity of 3.5 × 10^{-3} S cm^{-1}, while other three mixed-valence salts exhibit conductivity around 1.5 × 10^{-4} S cm^{-1}. The conductivity observed in the mixed-valence salt of **62b** is closely related to the p-type semiconductor behavior exhibited by a butylated derivative of **62b** in single-crystal transistors, which achieves a field-effect mobility of 0.37 cm^2 V^{-1} s^{-1}.[113]

5. Conclusions and outlook

The exploration of robust, fully characterized π-conjugated radical cations reveals a clear evolutionary path in their stabilization and application. While early strategies relied heavily on steric protection to isolate radical cations of simple polycyclic arenes, this approach often comes at the cost of electronic communication in the solid state, limiting its utility for functional materials. A more powerful paradigm has emerged through the use of π-units, such as phenalenyl, flattened triarylamines, and TTF, which confer thermodynamic stability by efficiently delocalizing spin and charge. This fundamental insight has been pivotal, enabling the development of organic conductors and semiconductors with high conductivity[114] without sacrificing intermolecular interactions. The recent identification of promising new motifs, such as double (hetero) helicenes and conjugated macrocycles, further enriches this toolkit for intrinsic stabilization.

In p-type organic semiconductors, the neutral molecule represents the undoped state, enabling high on–off ratios in OFETs, while the radical cations (including mixed-valence states) constitute the doped, higher-conductivity state. However, studies on the neutral and radical cation forms of the same π-system are often conducted in isolation. Only a handful of systems, such as TMTP (Fig. 1), **17a** (Fig. 6), and **59a** (Fig. 19), have been investigated in both states, typically using field-effect transistors for the neutral form and two-terminal devices for the radical cation. Bridging these largely separate research domains is a promising direction for future research. π-Systems proven in conductive radical cation salts could inspire design of new high-mobility semiconductors for OFETs. Simultaneously, robust radical cations from high-mobility neutral semiconductors offer a direct pathway to novel, highly conductive organic materials. A concerted effort to explore both states of the same molecular core will provide deeper insights into organic semiconductor design and accelerate the development of new materials.

Author contributions

S. Su and Q. Miao wrote the manuscript, and Q. Miao revised the manuscript according to the reviewers' comments.

Conflicts of interest

There are no conflicts to declare.

Data availability

No primary research results have been included, and no new data were generated or analyzed as a part of this review article.

Acknowledgements

This research was supported by the Research Grants Council of Hong Kong (CRF C4001-23G) and the State Key Laboratory of Synthetic Chemistry.

Notes and references

1 N. L. Bauld, in *Radicals, Ion Radicals, and Triplets*, Wiley-VCH, New York, 1997, p. 141.
2 Y. Shirota and H. Kageyama, *Chem. Rev.*, 2007, **107**, 953–1010.
3 F. Wudl, G. M. Smith and E. J. Hufnagel, *J. Chem. Soc. D*, 1970, 1453–1454.
4 F. Wudl, D. Wobschall and E. J. Hufnagel, *J. Am. Chem. Soc.*, 1972, **94**, 670–672.
5 H. Urayama, H. Yamochi, G. Saito, K. Nozawa, T. Sugano, M. Kinoshita, S. Sato, K. Oshima, A. Kawamoto and J. Tanaka, *Chem. Lett.*, 1988, **17**, 55–58.
6 B. Dhara, M. Nakamura, K. Bulgarevich and K. Takimiya, *Cryst. Growth Des.*, 2024, **24**, 5826–5833.
7 G. Heywang and S. Roth, *Angew Chem. Int. Ed. Engl.*, 1991, **30**, 176–177.
8 K. Takimiya, K. Bulgarevich, M. Abbas, S. Horiuchi, T. Ogaki, K. Kawabata and A. Ablat, *Adv. Mater.*, 2021, **33**, e2102914.

9 U. Geiser and J. A. Schlueter, *Chem. Rev.*, 2004, **104**, 5203–5242.
10 T. Sugawara, H. Komatsu and K. Suzuki, *Chem. Soc. Rev.*, 2011, **40**, 3105–3118.
11 Z. Mi, P. Yang, R. Wang, J. Unruangsri, W. Yang, C. Wang and J. Guo, *J. Am. Chem. Soc.*, 2019, **141**, 14433–14442.
12 M. Imran, C. M. Wehrmann and M. S. Chen, *J. Am. Chem. Soc.*, 2020, **142**, 38–43.
13 Z. X. Chen, Y. Li and F. Huang, *Chem*, 2021, **7**, 288–332.
14 D. Yuan, W. Liu and X. Zhu, *Chem*, 2021, **7**, 333–357.
15 S. Dong and Z. Li, *J. Mater. Chem. C*, 2022, **10**, 2431–2449.
16 L. Ji, J. Shi, J. Wei, T. Yu and W. Huang, *Adv. Mater.*, 2020, **32**, e1908015.
17 Q. Peng, A. Obolda, M. Zhang and F. Li, *Angew. Chem., Int. Ed.*, 2015, **54**, 7091–7095.
18 W. Zeng and J. Wu, *Chem*, 2021, **7**, 358–386.
19 B. Tang, J. Zhao, J. F. Xu and X. Zhang, *Chem. Sci.*, 2020, **11**, 1192–1204.
20 Z. Cui, A. Abdurahman, X. Ai and F. Li, *CCS Chem.*, 2020, **2**, 1129–1145.
21 F. Tani, M. Narita and T. Murafuji, *ChemPlusChem*, 2020, **85**, 2093–2104.
22 T. Harimoto and Y. Ishigaki, *ChemPlusChem*, 2022, **87**, e202200013.
23 W. Wang, P. Sun, X. Liu, X. Zhang, L. Zhang, Y. Z. Tan and X. Wang, *Org. Lett.*, 2024, **26**, 1017–1021.
24 P. T. Herwig, V. Enkelmann, O. Schmelz and K. Müllen, *Chem. – Eur. J.*, 2000, **6**, 1834–1839.
25 M. Banerjee, S. V. Lindeman and R. Rathore, *J. Am. Chem. Soc.*, 2007, **129**, 8070–8071.
26 J. Guo, C. Zhou, S. Xie, S. Luo, T. Y. Gopalakrishna, Z. Sun, J. Jouha, J. Wu and Z. Zeng, *Chem. Mater.*, 2020, **32**, 5927–5936.
27 H. Hayashi, J. E. Barker, A. Cardenas Valdivia, R. Kishi, S. N. MacMillan, C. J. Gomez-Garcia, H. Miyauchi, Y. Nakamura, M. Nakano, S. I. Kato, M. M. Haley and J. Casado, *J. Am. Chem. Soc.*, 2020, **142**, 20444–20455.
28 T. Nishinaga, K. Komatsu, N. Sugita, H. J. Lindner and J. Richter, *J. Am. Chem. Soc.*, 1991, **115**, 11642–11643.
29 P. L. Magueres, S. V. Lindeman and J. K. Kochi, *Org. Lett.*, 2000, **2**, 3567–3570.
30 T. Horibe, S. Ohmura and K. Ishihara, *J. Am. Chem. Soc.*, 2019, **141**, 1877–1881.
31 Y. Zhang, S. H. Pun and Q. Miao, *Chem. Rev.*, 2022, **122**, 14554–14593.
32 T. Kubo, Y. Goto, M. Uruichi, K. Yakushi, M. Nakano, A. Fuyuhiro, Y. Morita and K. Nakasuji, *Chem.–Asian J.*, 2007, **2**, 1370–1379.
33 C. M. Wehrmann, R. T. Charlton and M. S. Chen, *J. Am. Chem. Soc.*, 2019, **141**, 3240–3248.
34 G. Xie, V. Brosius, J. Han, F. Rominger, A. Dreuw, J. Freudenberg and U. H. F. Bunz, *Chem. – Eur. J.*, 2020, **26**, 160–164.
35 C. Sato, S. Suzuki, K. Okada and M. Kozaki, *Chem.–Asian J.*, 2018, **13**, 3729–3736.
36 M. Harada, M. Tanioka, A. Muranaka, T. Aoyama, S. Kamino and M. Uchiyama, *Chem. Commun.*, 2020, **56**, 9565–9568.
37 Y. K. Loh, P. Vasko, C. McManus, A. Heilmann, W. K. Myers and S. Aldridge, *Nat. Commun.*, 2021, **12**, 7052.
38 M. Narita, T. Teraoka, T. Murafuji, Y. Shiota, K. Yoshizawa, S. Mori, H. Uno, S. Kanegawa, O. Sato, K. Goto and F. Tani, *Bull. Chem. Soc. Jpn.*, 2019, **92**, 1867–1873.
39 C. Zhu, K. Shoyama and F. Wurthner, *Angew. Chem., Int. Ed.*, 2020, **59**, 21505–21509.
40 Y. Wang, Q. Gong, S. H. Pun, H. K. Lee, Y. Zhou, J. Xu and Q. Miao, *J. Am. Chem. Soc.*, 2022, **144**, 16612–16619.
41 L. Zhang, M. Gao, S. Su, Z. Zhou, H. K. Lee, X. Chen, Z. Huang and Q. Miao, *Chem. – Eur. J.*, 2025, **31**, e202501062.
42 A. Ito, Y. Ono and K. Tanaka, *Angew. Chem., Int. Ed.*, 2000, **39**, 1072–1075.
43 C. Wurster and E. Schobig, *Ber. Dtsch. Chem. Ges.*, 1879, **12**, 1807–1813.
44 E. T. Seo, R. F. Nelson, J. M. Fritsch, L. S. Marcoux, D. W. Leedy and R. N. Adams, *J. Am. Chem. Soc.*, 1966, **88**, 3498–3503.
45 M. Kuratsu, M. Kozaki and K. Okada, *Angew. Chem., Int. Ed.*, 2005, **44**, 4056–4058.
46 S. I. Kato, T. Matsuoka, S. Suzuki, M. S. Asano, T. Yoshihara, S. Tobita, T. Matsumoto and C. Kitamura, *Org. Lett.*, 2020, **22**, 734–738.
47 S. Kataoka, S. Suzuki, Y. Shiota, K. Yoshizawa, T. Matsumoto, M. S. Asano, T. Yoshihara, C. Kitamura and S. I. Kato, *J. Org. Chem.*, 2021, **86**, 12559–12568.
48 J. Borstelmann, V. Gensch, D. Fehn, M. E. Miehlich, F. Hampel, F. Rominger, K. Meyer and M. Kivala, *Angew. Chem., Int. Ed.*, 2025, **64**, e202423802.
49 X. Zheng, X. Wang, Y. Qiu, Y. Li, C. Zhou, Y. Sui, Y. Li, J. Ma and X. Wang, *J. Am. Chem. Soc.*, 2013, **135**, 14912–14915.
50 T. A. Schaub, T. Mekelburg, P. O. Dral, M. Miehlich, F. Hampel, K. Meyer and M. Kivala, *Chem. – Eur. J.*, 2020, **26**, 3264–3269.
51 D. Sakamaki, D. Kumano, E. Yashima and S. Seki, *Chem. Commun.*, 2015, **51**, 17237–17240.
52 K. Harada, C. Hasegawa, T. Matsumoto, H. Sugishita, C. Kitamura, S. Higashibayashi, M. Hasegawa, S. Suzuki and S. I. Kato, *Chem. Commun.*, 2023, **59**, 1301–1304.
53 D. Sakamaki, S. Tanaka, K. Tanaka, M. Takino, M. Gon, K. Tanaka, T. Hirose, D. Hirobe, H. M. Yamamoto and H. Fujiwara, *J. Phys. Chem. Lett.*, 2021, **12**, 9283–9292.
54 D. Sakamaki, H. Sekiguchi, S. Suzuki and H. Fujiwara, *Chem. – Eur. J.*, 2025, **31**, e202500942.
55 L. Ruan, R. Li, M. Li, Y. Huang and P. An, *J. Org. Chem.*, 2025, **90**, 4365–4373.
56 G. Xie, N. M. Bojanowski, V. Brosius, T. Wiesner, F. Rominger, J. Freudenberg and U. H. F. Bunz, *Chem. – Eur. J.*, 2021, **27**, 1976–1980.
57 B. Huang, H. Kang, X.-L. Zhao, H.-B. Yang and X. Shi, *Cryst. Growth Des.*, 2022, **22**, 3587–3593.
58 X. Gu, B. Shan, Z. He and Q. Miao, *ChemPlusChem*, 2017, **82**, 1034–1038.

59 L. Zhang, Y. Zhao, J. Li, Y. Fu, B. Peng, J. Yang, X. Lu and Q. Miao, *J. Am. Chem. Soc.*, 2025, **147**, 3459–3467.
60 L. Li, Y. Su, Y. Ji and P. Wang, *J. Am. Chem. Soc.*, 2023, **145**, 5778–5785.
61 H.-P. J. de Rouville, C. Gourlaouen, D. Bardelang, N. Le Breton, J. S. Ward, L. Ruhlmann, J. M. Vincent, D. Jardel, K. Rissanen, J. L. Clement, S. Choua and V. Heitz, *J. Am. Chem. Soc.*, 2025, **147**, 1823–1830.
62 Q. Qi, P. M. Burrezo, H. Phan, T. S. Herng, T. Y. Gopalakrishna, W. Zeng, J. Ding, J. Casado and J. Wu, *Chem. – Eur. J.*, 2017, **23**, 7595–7606.
63 Y. Matsuo, T. Tanaka and A. Osuka, *Chem. – Eur. J.*, 2020, **26**, 8144–8152.
64 H. Yokoi, S. Hiroto and H. Shinokubo, *J. Am. Chem. Soc.*, 2018, **140**, 4649–4655.
65 T. Nishinaga, A. Wakamiya, D. Yamazaki and K. Komatsu, *J. Am. Chem. Soc.*, 2004, **126**, 3163–3174.
66 D. Yamazaki, T. Nishinaga, N. Tanino and K. Komatsu, *J. Am. Chem. Soc.*, 2006, **128**, 14470–14471.
67 T. Fujiwara, A. Muranaka, T. Nishinaga, S. Aoyagi, N. Kobayashi, M. Uchiyama, H. Otani and M. Iyoda, *J. Am. Chem. Soc.*, 2020, **142**, 5933–5937.
68 T. Fujiwara, M. Takashika, M. Hasegawa, Y. Ie, Y. Aso, S. Aoyagi, H. Otani and M. Iyoda, *ChemPlusChem*, 2019, **84**, 694–703.
69 Y. Kobayashi, T. Terauchi, S. Sumi and Y. Matsushita, *Nat. Mater.*, 2017, **16**, 109–114.
70 M. Vicent-Morales, M. Esteve-Rochina, J. Calbo, E. Orti, I. J. Vitorica-Yrezabal and G. Minguez Espallargas, *J. Am. Chem. Soc.*, 2022, **144**, 9074–9082.
71 A. Trabolsi, N. Khashab, A. C. Fahrenbach, D. C. Friedman, M. T. Colvin, K. K. Coti, D. Benitez, E. Tkatchouk, J. C. Olsen, M. E. Belowich, R. Carmielli, H. A. Khatib, W. A. Goddard, M. R. Wasielewski and J. F. Stoddart, *Nat. Chem.*, 2010, **2**, 42–49.
72 A. C. Fahrenbach, J. C. Barnes, D. A. Lanfranchi, H. Li, A. Coskun, J. J. Gassensmith, Z. Liu, D. Benitez, A. Trabolsi, W. A. Goddard, M. Elhabiri and J. F. Stoddart, *J. Am. Chem. Soc.*, 2012, **134**, 3061–3072.
73 A. C. Fahrenbach, S. Sampath, D. J. Late, J. C. Barnes, S. L. Kleinman, N. Valley, K. J. Hartlieb, Z. Liu, V. P. Dravid, G. C. Schatz, R. P. Van Duyne and J. F. Stoddart, *ACS Nano*, 2012, **6**, 9964–9971.
74 Y. Jiao, Y. Qiu, L. Zhang, W. G. Liu, H. Mao, H. Chen, Y. Feng, K. Cai, D. Shen, B. Song, X. Y. Chen, X. Li, X. Zhao, R. M. Young, C. L. Stern, M. R. Wasielewski and R. D. Astumian, *Nature*, 2022, **603**, 265–270.
75 Y. Jiao, H. Mao, Y. Qiu, G. Wu, H. Chen, L. Zhang, H. Han, X. Li, X. Zhao, C. Tang, X. Y. Chen, Y. Feng, C. L. Stern, M. R. Wasielewski and J. F. Stoddart, *J. Am. Chem. Soc.*, 2022, **144**, 23168–23178.
76 H. Han, Y. Huang, C. Tang, Y. Liu, M. D. Krzyaniak, B. Song, X. Li, G. Wu, Y. Wu, R. Zhang, Y. Jiao, X. Zhao, X. Y. Chen, H. Wu, C. L. Stern, Y. Ma, Y. Qiu, M. R. Wasielewski and J. F. Stoddart, *J. Am. Chem. Soc.*, 2023, **145**, 18402–18413.
77 L. Mao, M. Zhou, T. Wu, D. Ma, G. Dai and X. Shi, *Org. Lett.*, 2024, **26**, 7244–7248.
78 H. Morishita, K. Sambe, S. Dekura, H. Sugishita, C. Kitamura, T. Matsumoto, T. Takeda, R. Uesugi, T. Ishida, T. Akutagawa, S. Suzuki and S. I. Kato, *Chem. – Eur. J.*, 2025, **31**, e202500576.
79 J. Borstelmann, S. Zank, M. Krug, G. Berger, N. Frohlich, G. Glotz, F. Gnannt, L. Schneider, F. Rominger, F. Deschler, T. Clark, G. Gescheidt, D. M. Guldi and M. Kivala, *Angew. Chem., Int. Ed.*, 2025, **64**, e202423516.
80 R. Kurata, D. Sakamaki and A. Ito, *Org. Lett.*, 2017, **19**, 3115–3118.
81 W. Wang, L. Wang, S. Chen, W. Yang, Z. Zhang and X. Wang, *Sci. China Chem.*, 2017, **61**, 300–305.
82 W. Wang, C. Chen, C. Shu, S. Rajca, X. Wang and A. Rajca, *J. Am. Chem. Soc.*, 2018, **140**, 7820–7826.
83 S. Dong, T. Y. Gopalakrishna, Y. Han and C. Chi, *Angew. Chem., Int. Ed.*, 2019, **58**, 11742–11746.
84 Y. Ma, Y. Han, X. Hou, S. Wu and C. Chi, *Angew. Chem., Int. Ed.*, 2024, **63**, e202407990.
85 Z. Li, X. Hou, Y. Han, W. Fan, Y. Ni, Q. Zhou, J. Zhu, S. Wu, K. W. Huang and J. Wu, *Angew. Chem., Int. Ed.*, 2022, **61**, e202210697.
86 Y. D. Yang, M. Leng, Q. Zhang, X. Jin, C. V. Chau, J. Yang, S. Vasylevskyi, G. Henkelman, H. Y. Gong, L. Fang and J. L. Sessler, *J. Am. Chem. Soc.*, 2025, **147**, 19364–19371.
87 Y. D. Yang, Q. Zhang, L. Khrouz, C. V. Chau, J. Yang, Y. Wang, C. Bucher, G. Henkelman, H. Y. Gong and J. L. Sessler, *ACS Cent. Sci.*, 2024, **10**, 1148–1155.
88 H. Wei, X. Hou, T. Xu, Y. Zou, G. Li, S. Wu, Y. Geng and J. Wu, *Angew. Chem., Int. Ed.*, 2022, **61**, e202210386.
89 S. Arikawa, A. Shimizu, D. Shiomi, K. Sato, T. Takui, H. Sotome, H. Miyasaka, M. Murai, S. Yamaguchi and R. Shintani, *Angew. Chem., Int. Ed.*, 2023, **62**, e202302714.
90 M. Ahmed, Y. Wu, M. R. Schiavone, K. Lang, L. You, M. Zeller and J. Mei, *Org. Lett.*, 2023, **25**, 6363–6367.
91 S. Tang, L. Zhang, H. Ruan, Y. Zhao and X. Wang, *J. Am. Chem. Soc.*, 2020, **142**, 7340–7344.
92 H. P. Fritz, H. Gebauer, P. Friedrich, P. Ecker, R. Artes and U. Schubert, *Z. Naturforsch., B: Chem. Sci.*, 1978, **33**, 498–506.
93 G. Saito and T. Murata, *Philos. Trans. R. Soc., A*, 2008, **366**, 139–150.
94 A. Schätzle, J. U. Von SchÜTz, H. C. Wolf, H. Schäfer and H. W. Helberg, *Mol. Cryst. Liq. Cryst.*, 1985, **120**, 229–232.
95 H. J. Keller, D. Nöthe, H. Pritzkow, D. Wehe, M. Werner, P. Koch and D. Schweitzer, *Mol. Cryst. Liq. Cryst.*, 1980, **62**, 181–199.
96 P. Koch, D. Schweitzer, R. H. Harms, H. J. Keller, H. Schäfer, H. W. Helberg, R. Wilckens, H. P. Geserich and W. Ruppel, *Mol. Cryst. Liq. Cryst.*, 1982, **86**, 87–101.
97 H. Endres, H. J. Keller, B. Müller and D. Schweitzer, *Acta Crystallogr., Sect. C: Cryst. Struct. Commun.*, 1985, **41**, 607–613.
98 C. Kröhnke, V. Enkelmann and G. Wegner, *Angew Chem. Int. Ed. Engl.*, 1980, **19**, 912–919.
99 J. Ferraris, D. O. Cowan, V. Walatka and J. H. Perlstein, *J. Am. Chem. Soc.*, 1973, **95**, 948–949.

100 R. Comès, S. M. Shapiro, G. Shirane, A. F. Garito and A. J. Heeger, *Phys. Rev. Lett.*, 1975, **35**, 1518–1521.
101 T. E. Phillips, T. J. Kistenmacher, J. P. Ferraris and D. O. Cowan, *J. Chem. Soc., Chem. Commun.*, 1973, 471–472.
102 D. Jérome, A. Mazaud, M. Ribault and K. Bechgaard, *J. Phys., Lett.*, 1980, **41**, 95–98.
103 K. Bechgaard, K. Carneiro, M. Olsen, F. B. Rasmussen and C. S. Jacobsen, *Phys. Rev. Lett.*, 1981, **46**, 852–855.
104 M. A. Christensen, C. R. Parker, T. J. Sørensen, S. de Graaf, T. J. Morsing, T. Brock-Nannestad, J. Bendix, M. M. Haley, P. Rapta, A. Danilov, S. Kubatkin, O. Hammerich and M. B. Nielsen, *J. Mater. Chem. C*, 2014, **2**, 10428–10438.
105 L. Feng, H. Dong, Q. Li, W. Zhu, G. Qiu, S. Ding, Y. Li, M. A. Christensen, C. R. Parker, Z. Wei, M. B. Nielsen and W. Hu, *Sci. China Mater.*, 2016, **60**, 75–82.
106 J. Xu, Q. Chen, S. Li, J. Shen, P. Keoingthong, L. Zhang, Z. Yin, X. Cai, Z. Chen and W. Tan, *Angew. Chem., Int. Ed.*, 2022, **61**, e202202571.
107 G. Liu, L. Gao, Y. Han, Y. Xiao, B. Du, J. Gong, J. Hu, F. Zhang, H. Meng, X. Li, X. Shi, Z. Sun, J. Wang, G. Dai, C. Chi and Q. Wang, *Angew. Chem., Int. Ed.*, 2023, **62**, e202301348.
108 O. Matuszewska, T. Battisti, R. R. Ferreira, N. Biot, N. Demitri, C. Meziere, M. Allain, M. Salle, S. Manas-Valero, E. Coronado, E. Fresta, R. D. Costa and D. Bonifazi, *Chem. – Eur. J.*, 2023, **29**, e202203115.
109 N. Kobayashi, M. Sasaki and K. Nomoto, *Chem. Mater.*, 2009, **21**, 552–556.
110 L. Ethordevic, C. Valentini, N. Demitri, C. Meziere, M. Allain, M. Salle, A. Folli, D. Murphy, S. Manas-Valero, E. Coronado and D. Bonifazi, *Angew. Chem., Int. Ed.*, 2020, **59**, 4106–4114.
111 Y. Gao, Z. Liu, T. Li and W. Zhao, *Angew. Chem., Int. Ed.*, 2023, **62**, e202314006.
112 L. Wu, Y. Li, X. Hua, L. Ye, C. Yuan, Z. Liu, H. L. Zhang and X. Shao, *Angew. Chem., Int. Ed.*, 2024, **63**, e202319587.
113 B. Fu, X. Hou, C. Wang, Y. Wang, X. Zhang, R. Li, X. Shao and W. Hu, *Chem. Commun.*, 2017, **53**, 11407–11409.
114 M. Ikeda, Y. Sasaki, Y. Fujikawa, S. Mori, K. Konishi, K. Ohara, H. Dekura, H. Toyota, M. Takase, A. Mi Shirai, Y. Murotani, R. Matsunaga and T. Naito, *J. Mater. Chem. C*, 2025, **13**, 12650–12656.